CHALMERS
UNIVERSITY OF TECHNOLOGY

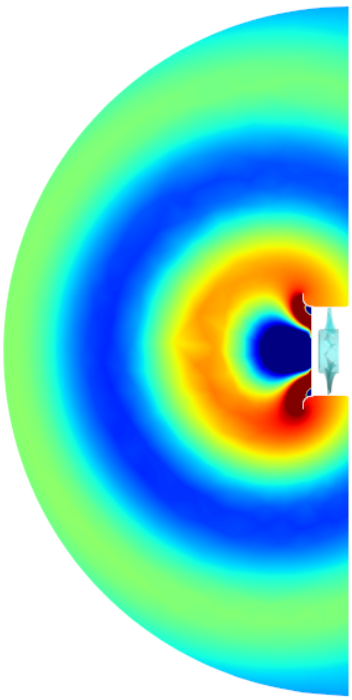

Numerical Investigation of Noise Generation by Automotive Cooling Fans

Master's thesis in Sustainable Energy Systems

OMAR FARES

Department of Mechanics and Maritime Science
CHALMERS UNIVERSITY OF TECHNOLOGY
Gothenburg, Sweden 2019

Master's thesis 2019:90

Numerical Investigation of Noise Generation by Automotive Cooling Fans

OMAR FARES

CHALMERS
UNIVERSITY OF TECHNOLOGY

Department of Mechanics and Maritime Science
Division of Fluid Dynamics
Chalmers University of Technology
Gothenburg, Sweden 2019

Numerical Investigation of Noise Generation by Automotive Cooling Fans

Supervisor: Chenyang Weng, Volvo Cars Group
Hua-Dong Yao, Department of Mechanics and Maritime Science
Lars Davidson, Department of Mechanics and Maritime Science

Examiner: Lars Davidson, Department of Mechanics and Maritime Science
Hua-Dong Yao, Department of Mechanics and Maritime Science

Master's Thesis 2019:90
Department of Mechanics and Maritime Science
Division of Fluid Dynamics
Chalmers University of Technology
SE-412 96 Gothenburg
Telephone +46 31 772 1000

Typeset in LaTeX
Printed by [Reproservice/Department of Applied Mechanics]
Gothenburg, Sweden 2019

Numerical Investigation of Noise Generation by Automotive Cooling Fans
OMAR FARES
Department of Mechanics and Maritime Science
Chalmers University of Technology

Abstract

Electrical vehicle technology is sharply rising and expected to dominate the international market in the coming 10 years. In electric vehicles, axial cooling fans are commonly used to cool batteries with high heating load. One drawback of axial cooling fans is the high aeroacoustic noise level resulting from the fan blades and the obstacles facing the air flow. To create a comfortable cabin environment in the vehicle, a low-noise installation design of the axial fan is required. The purpose of the current project is to develop an efficient computational aeroacoustics (CAA) simulation process to assist the cooling-fan installation design.
The current thesis focuses on a hybrid CAA approach where the aerodynamic field is obtained through the unsteady Reynolds-averaged Navier-Stokes equations (URANS) model, and the acoustic field is computed via Lighthill's analogy. The simulation process is applied to a benchmark case in the literature, where the aerodynamics and aeroacoustics of a low-speed axial fan are investigated separately. Initial steady state simulation is performed using the moving reference frame (MRF) approach to quantify different simulation model parameters before running the main URANS simulation. The URANS model provides good prediction of the mean flow quantities. The computed unsteady wall pressure fluctuations succeeds to resolve the fan blade passing frequency and the sub-harmonic frequency resulted from the interaction of the gap flow with the fan blades.
The CAA approach studied in this thesis is limited to the prediction of narrow-band components of the fan noise, i.e., the blade-passing-frequency (BPF) noise and the noise generated by distinct coherent vortex structures. The aeroacoustic simulation model successfully captures the narrow-band acoustic signal and gives promising results for extending the approach to predict broad-band fan noise by replacing the URANS model with more advanced CFD models, such as the large eddy simulation.

Keywords: Computational Fluid Dynamics (CFD), Aeroacoustics, Low-speed axial fan, Unsteady Reynold averaged Navier-Stokes equations (URANS), Lighthill's analogy, Sound propagation, Star-CCM+, Actran.

Acknowledgements

The presented Master's thesis project was carried out during the spring of 2019 at the NVH Driving Dynamics Centre at Volvo Car Group. This work would not have been possible with out the unlimited support from my supervisor Chenyang Weng which I would like to express my deep and sincere gratitude to him for his patience, immense knowledge and motivation throughout the whole project. It was a great privilege and honour to work and study under his guidance. I am also grateful to Linus Zackrisson for his continuous guidance and for teaching me valuable information about CFD methodologies in Star-CCM+. I am also thankful to Asuka Pietroniro and all of those whom I have had the pleasure to work with in the department during my project. A special thanks goes to my Group Manager Magnus Knutsson for his persistent follow up and support to the project and for allocating all the resources needed for me to complete the project.
Furthermore, I would like to thank my university supervisors and examiners Hua-Dong Yao and Prof.Lars Davidson for their insightful discussions and feedback comments. I would like also to thank CD-adapco assistance and in particular Jeremy Dahan for sharing his ideas with us regarding implementations methods that can be applied by Star-CCM+. In addition, the FFT assistant staff (Thanos, Maxime, Cyril, Kauê, Leonidas, and Diego) are appreciated for their support with the acoustic simulation software Actran.
Finally, I would like to thank my family for being always there for me during the hard times of my studies.

Omar Fares, Gothenburg, August 2019

Contents

List of Figures xi

List of Tables xiii

1 Introduction 1
- 1.1 Background . . . 1
- 1.2 Purpose . . . 1
- 1.3 Limitations . . . 1
- 1.4 Methodology . . . 2

2 Theory 3
- 2.1 Governing equations . . . 3
- 2.2 Turbulent flow . . . 4
  - 2.2.1 Turbulence modeling . . . 5
    - 2.2.1.1 The realizable $k-\varepsilon$ model . . . 6
    - 2.2.1.2 The SST $k-\omega$ model . . . 7
  - 2.2.2 Boundary layer . . . 7
- 2.3 Numerical methods for CFD . . . 9
  - 2.3.1 Finite volume method . . . 9
  - 2.3.2 Spatial discretization schemes . . . 11
    - 2.3.2.1 First-order upwind . . . 11
    - 2.3.2.2 Second-order upwind . . . 11
  - 2.3.3 Temporal discretization scheme . . . 11
  - 2.3.4 Measuring convergence . . . 12
- 2.4 Fan modelling . . . 12
  - 2.4.1 Moving reference frame . . . 12
- 2.5 Aeroacoustics . . . 13
  - 2.5.1 Acoustic wave equation . . . 14
  - 2.5.2 Lighthill's analogy . . . 14

3 Simulation setup 17
- 3.1 CFD simulation . . . 17
  - 3.1.1 Geometry . . . 17
  - 3.1.2 Volume meshing . . . 17
    - 3.1.2.1 Prism layer . . . 18
    - 3.1.2.2 Core volume mesh . . . 20
  - 3.1.3 Boundary conditions . . . 21

3.1.4 Physics . . . 21
3.1.5 Solver settings . . . 22
3.1.5.1 Pressure-velocity coupling . . . 22
3.1.5.2 Coupled and segregated flow solvers . . . 22
3.1.5.3 Discretization schemes and time step . . . 23
3.1.6 Measuring points . . . 23
3.1.6.1 Velocity and wall pressure fluctuations . . . 23
3.2 Acoustic simulation . . . 23
3.2.1 Surface noise source . . . 24
3.2.2 Volume mesh and boundary conditions . . . 25
3.2.3 Measuring points . . . 26

4 Results & Discussion **27**
4.1 Steady state simulation . . . 27
4.1.1 Pressure difference . . . 27
4.1.2 Axial velocity . . . 28
4.2 Unsteady state simulation . . . 29
4.2.1 Pressure difference . . . 29
4.2.2 Axial velocity . . . 29
4.2.3 Wall pressure fluctuations . . . 31
4.3 CAA simulation . . . 32

5 Conclusion **35**

Bibliography **37**

A Appendix: Comparison among different wall treatments in RANS models **I**

B Appendix: Blade element/momentum method (BEMM) **III**
B.1 Theory . . . III
B.2 Implementation . . . IV
B.3 Application to N1UG fan . . . V

List of Figures

1.1 Schematic overview of the project workflow. 2

2.1 Sub-layers at inner region. 8
2.2 One dimensional domain describing neighboring cells and cell faces. . 10
2.3 Comparison between moving and stationery reference frames. 13

3.1 Fan pressure side, before and after cleaning. 18
3.2 Fan suction side, before and after cleaning. 18
3.3 CFD computational domain and the coordinate system followed . . . 19
3.4 Prism layer specific properties. 19
3.5 y^+ contour at rotor blades. 20
3.6 Mesh structure cross section. 20
3.7 Flow field measuring points. 23
3.8 New surface source position highlighted in dark green. 24
3.9 Velocity contour of different surface sources. 24
3.10 Mesh structure cross section. 25
3.11 Computational domain top view. 25

4.1 Axial mean velocity profile $\langle U_x \rangle$ for different turbulence models. . . . 28
4.2 Axial velocity profile $\langle U_x \rangle$ for different mesh structures. 29
4.3 Axial velocity profile $\langle U_x \rangle$ for different mesh refinements. 29
4.4 Time averaged axial velocity profile for different turbulence models. . 30
4.5 Time averaged axial velocity profile for different mesh structures. . . 31
4.6 PSD of wall pressure probes at the fan duct. 32
4.7 PSD of the acoustic signal. 33
4.8 Lighthill surface density at 335Hz. 33

A.1 Two mesh setups used in the test case. II
A.2 Dimensionless velocity $u^+ = u/u_*$ over y^+. Note that the SST $k-\omega$ model with low y^+ treatment is not converged in the case of Fig. A.2(b). II

B.1 Sketch of the velocity triangle and force vector on a blade element. Image source: [1], reproduced with permission. III

List of Tables

3.1 Mesh models properties. 20
3.2 Physics models. 22

4.1 Pressure difference for different steady simulation models. 27
4.2 Pressure difference for different unsteady simulation models. 30

B.1 Comparison between the N1UG design parameters given in [2] and those reversely computed with the current implementation of the BEMM [1]. The chord lengths are different in the two cases mainly due to the choices of the blade element sizes. V

1
Introduction

1.1 Background

Electric vehicles (EVs) are the future. An important problem of the existing cooling systems for EVs is the significant noise emission while charging the batteries of electric motors. The noise can propagate outside and introduce obvious pollution to the neighborhood. Besides, the creation of comfortable cabin environments is always concerned in the automotive industry to boost the competitive power of productions. There is therefore an demand to develop quiet and efficient cooling systems. To reduce product development cost and time, building an robust numerical tool for the fan-noise prediction is beneficial.

Several numerical approaches for fan-noise prediction can be found in literature. For example, the Ffowcs Williams-Hawkings equation is used by Khelladi et al. [3] to predict dipole and monopole tonal noises from a high rotational speed centrifugal fan; the variational form of the Lighthill's analogy is used by Rynell et al. [4] to study both the narrow-band and broadband noise of an axial cooling fan; the acoustic perturbation equations are used by Kaltenbacher et al. [5], Junger et al. [6] to study the aeroacoustic properties of an axial fan. The choice of the numerical method depends on many factors, such as the requirement of simulation accuracy and time, the availability of software, etc.

1.2 Purpose

The purpose of this thesis is to set up computational fluid dynamics (CFD) and computational aeroacoustic (CAA) model to simulate the flow and sound field of an axial fan. Simulation results would be validated by the experimentally measured data provided by Zenger [2] as a benchmark case.

1.3 Limitations

This project is limited in time to 20 weeks for one MSc student. Computer resources including software and hardware are limited to those available at Volvo Cars Cooperation (VCC).

Due to the use of URANS, the current study can only predict narrow-band noise.

1.4 Methodology

In this section, project workflow of the simulation setup is described. Initially, a CAD file is supplied by Zenger et al. [2] for the benchmark case investigated, then imported to the pre-processing software ANSA for further simplification and computational domain creation. The simplified pre-processed surface mesh produced in ANSA is imported to the main CFD software Star-CCM+ to generate the volume mesh and set up the physics-model definitions, including material properties, flow and energy coupling, turbulence model and solver parameters. Boundary conditions are then defined for the computational domain before volume mesh generation. Steady and unsteady simulations are performed to evaluate different parameters and models to reach to the best simulation model. Acoustic mesh is then prepared using ANSA and exported to the acoustic software Actran where the CFD computations exported from Star-CCM+ are mapped to the acoustic mesh and the sound field is solved through the Lighthill's analogy. Finally, the acoustic results are post-processed and evaluated.

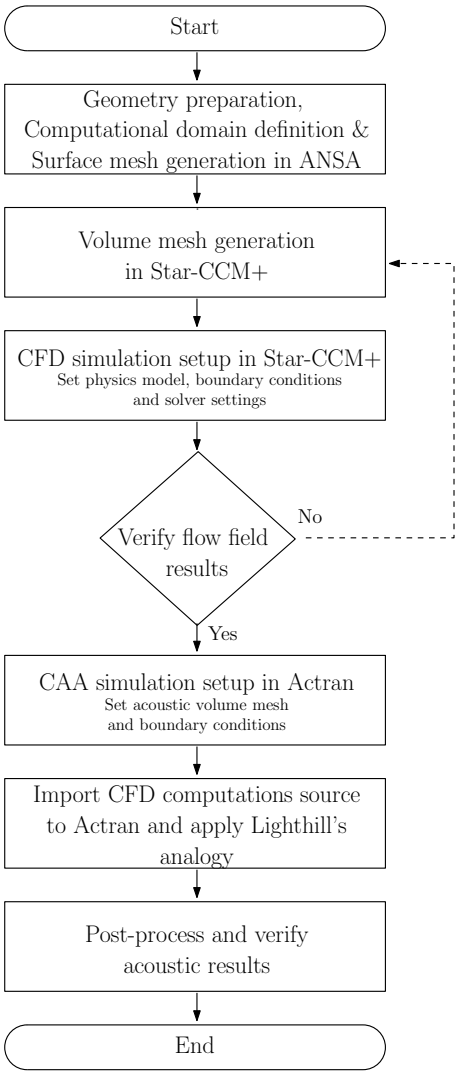

Figure 1.1: Schematic overview of the project workflow.

2

Theory

This chapter gives brief theoretical aspects involved in this thesis. First, a description of the governing equations of the fluid mechanics is given, followed by a summary of the turbulence modeling. Then, the CFD techniques used in this study are introduced, and the approach used to model the rotating behavior of the fan rotor is described. Finally, the Lighthill's analogy used to model the noise generation by the fan is described, and the relation between the Curle's analgy and the variational formulation of the Lighthill's analogy that is used in Actran is discussed.

2.1 Governing equations

To simulate any fluid flow, the physical properties of the fluid (density, velocity, etc..) need to be mathematically modeled. Depending on the scale of interest, one can model fluid flow differently. At microscopic level, fluid can be compromised as a group of individual molecules with non-uniform physical properties. However, the phenomena studied in fluid dynamics are generally macroscopic where the physical properties are assigned to different fluid grid elements containing a number of molecules. Compressible flow can be macroscopically modeled by the three continuum equations of conservation, i.e., the conservation of mass, conservation of momentum, and conservation of energy.
The conservation of mass leads to the continuity equation which describes the mass transport over a finite fluid element:

$$\frac{\partial \rho}{\partial t} + \frac{\partial \rho u_i}{\partial x_i} = Q_m, \tag{2.1}$$

where Q_m is introduced as a mass source term in the equation.
The momentum equation (the Navier-Stokes equation) is considered to be a statement of Newton's second law of motion which relates the sum of forces acting on a fluid element to its rate of motion and reads [7]

$$\frac{\partial \rho u_i}{\partial t} + \frac{\partial \rho u_j u_i}{\partial x_j} = -\frac{\partial p}{\partial x_i} + \frac{\partial \tau_{ij}}{\partial x_j} + f_i, \tag{2.2}$$

where f_i describes the external body forces and τ_{ij} is the viscous stress tensor which, for Newtonian fluid, is defined as:

$$\tau_{ij} = \mu\Big(\frac{\partial u_i}{\partial x_j} + \frac{\partial u_j}{\partial x_i}\Big) - (\frac{2}{3}\mu\frac{\partial u_k}{\partial x_k}\delta_{ij}), \tag{2.3}$$

where δ_{ij} is the Kronecker delta which has the value of 1 if $i = j$ and 0 if $i \neq j$.
The conservation equation of energy is a mathematical description of the first law of thermodynamics, which states that the rate of change of energy inside a fluid element is equal to the rate of energy received by heat and work to that fluid element. The equation is written as

$$\frac{\partial \rho e}{\partial t} + \frac{\partial \rho u_i e}{\partial x_i} = -p\frac{\partial u_i}{\partial x_i} + \tau_{ij}\frac{\partial u_i}{\partial x_j} + \frac{\partial}{\partial x_j}\Big(\kappa\frac{\partial T}{\partial x_j}\Big) + S_E, \tag{2.4}$$

where e is the internal energy and κ= κ(T) is the thermal conductivity and S_E is the energy source term.
For air at ambient conditions, the behavior of the gas is well approximated by the ideal gas law, which relates the pressure, density and temperature as follows,

$$p = \rho R T, \tag{2.5}$$

where R is the specific gas constant. Under such law, the internal energy e can be represented by the temperature T via

$$\mathrm{d}e = C_\mathrm{v}\mathrm{d}T, \tag{2.6}$$

where C_v is the specific heat capacity at constant volume.
Now the number of unknowns is equal to the number of equations, and the set of equations can be solved for a specific computational domain with proper initial and boundary conditions. For turbulent flow, solving the equations directly using direct numerical simulation (DNS) approach is usually computationally demanding. Therefore, different turbulence models have been developed to reduce the computational cost. The turbulence models used in this study is introduced in the next section.

2.2 Turbulent flow

According to Hinze[8] turbulence can be characterized as:

Turbulent fluid motion is an irregular condition of flow in which the various quantities show random variation with time and space coordinates, so the statistically distinct average values can be discerned

Turbulent flow is encountered in most engineering applications. Several models were introduced to model the flow in a less computational way. Depending on the level of information being interested in, different modeling approaches should be chosen. In this section, the turbulence modeling chosen in this study is described. The model is based on the Reynolds decomposition, i.e., the flow quantities are decomposed into their mean and fluctuating values as follows

$$u_i = \langle U_i \rangle + u_i', \tag{2.7}$$

$$p = \langle P \rangle + p', \tag{2.8}$$

where the mean values are defined as,

$$\langle \phi \rangle = \frac{1}{\tau} \int_{t}^{t+\tau} \phi(x,t) dt. \tag{2.9}$$

Applying the Reynolds decomposition to the incompressible version of the conservation equations yields the following time-averaged continuity equation (Eq. (2.10)), time-averaged Navier-Stokes equations which is commonly known as the unsteady Reynolds-averaged Navier-Stokes equations (Eq. (2.11)) (URANS) and the time-averaged energy equation (Eq. (2.12)) (with all the source terms neglected):

$$\frac{\partial \langle U_i \rangle}{\partial x_i} = 0, \tag{2.10}$$

$$\frac{\partial \langle U_i \rangle}{\partial t} + \langle U_j \rangle \frac{\partial \langle U_i \rangle}{\partial x_j} = -\frac{1}{\rho}\frac{\partial \langle P \rangle}{\partial x_i} + \nu \frac{\partial^2 \langle U_i \rangle}{\partial x_j \partial x_j} - \underbrace{\frac{\partial \langle u_i' u_j' \rangle}{\partial x_j}}_{\text{(i)}}, \tag{2.11}$$

$$\begin{aligned} &\frac{\partial \langle e \rangle}{\partial t} + \langle U_i \rangle \frac{\partial \langle e \rangle}{\partial x_i} \\ &= -\frac{1}{\rho}\frac{\partial \langle P \rangle \langle U_i \rangle}{\partial x_i} + \frac{\langle \tau_{ij} \rangle}{\rho}\frac{\partial \langle u_i \rangle}{\partial x_j} + \frac{1}{\rho}\frac{\partial}{\partial x_i}\Big(\kappa \frac{\partial \langle T \rangle}{\partial x_j}\Big) - \underbrace{\frac{\partial \langle u_i' e' \rangle}{\partial x_i}}_{\text{(ii)}}. \end{aligned} \tag{2.12}$$

In the above equations, there are two terms, (i) and (ii), which involve the average of the nonlinear turbulent fluctuations. The first term $\langle u_i' u_j' \rangle$ is known as the Reynolds stress tensor and appears as additional fictitious stresses that interact and affect the mean flow [7]. The second term $\langle u_i' e' \rangle$ is analogous in its definition to the Reynolds stress tensor but instead describes the turbulent heat flux vector. These two newly introduced terms should be further modeled in order to close the equation system. Because the internal energy is not interested in this study, and because the energy equation Eq. (2.12) is decoupled from the other conservation equations due to the assumption of incompressible flow, only Eq. (2.10) and Eq. (2.11) need to be solved in this study and hence only the modeling of (i) is introduced in the next section.

2.2.1 Turbulence modeling

Turbulence modeling is a way to relate the unclosed fluctuating terms to the dependent variable. One commonly used turbulence model is the so-called "eddy-viscosity model", which implements the Boussinesq approximation by relating the Reynolds stresses to the shear strain rate via the eddy viscosity ν_t [7]

$$\langle u_i' u_j' \rangle = -\nu_t \Big(\frac{\partial \langle U_i \rangle}{\partial x_j} + \frac{\partial \langle U_j \rangle}{\partial x_i} \Big) + \frac{2}{3} k \delta_{ij}, \tag{2.13}$$

where k is the turbulent kinetic energy per unit mass and defined as $k = \frac{1}{2}\langle u_i' u_i' \rangle$. There exists many methods for the determination of the eddy viscosity ν_t. These methods are classified by the number of transport equations added in addition to the

Reynolds averaged equations to determine the local eddy viscosity. In this section, only the classification of two-equation models is discussed.
In the two-equation models, the eddy viscosity can be described in term of the turbulent kinetic energy and another turbulent quantity. Two of the mostly used two-equation models, the realizable $k-\varepsilon$ model and the SST $k-\omega$ model, are summarized here.

2.2.1.1 The realizable $k-\varepsilon$ model

In this model, the turbulent quantity that is used to describe the eddy viscosity is the turbulent energy dissipation rate ε, defined by

$$\varepsilon = \frac{k^{\frac{3}{2}}}{l}. \tag{2.14}$$

where l is the characteristic length scale of the local turbulent eddies, and C_ν is a proportionality constant. The eddy viscosity then reads,

$$\nu_t = C_\mu \frac{k^2}{\varepsilon}, \tag{2.15}$$

The exact transport equations for ε and k are illustrated by Launder and Spalding[9] and written as

$$\frac{\partial k}{\partial t} + \langle U_i \rangle \frac{\partial k}{\partial x_i} = \frac{\partial}{\partial x_i}\Big[\Big(\nu + \frac{\nu_t}{\sigma_k}\Big)\frac{\partial k}{\partial x_i}\Big] + \nu_t \left[\left(\frac{\partial \langle U_i \rangle}{\partial x_j} + \frac{\partial \langle U_j \rangle}{\partial x_i}\right)\frac{\partial \langle U_i \rangle}{\partial x_j}\right] - \varepsilon. \tag{2.16}$$

$$\frac{\partial \varepsilon}{\partial t} + \frac{\partial \langle U_i \rangle \varepsilon}{\partial x_i} = \frac{\partial}{\partial x_i}\Big[\Big(\nu + \frac{\nu_t}{\sigma_\varepsilon}\Big)\frac{\partial \varepsilon}{\partial x_i}\Big] + \underbrace{\frac{\varepsilon}{k} C_{\varepsilon 1} \nu_t \left[\left(\frac{\partial \langle U_i \rangle}{\partial x_j} + \frac{\partial \langle U_j \rangle}{\partial x_i}\right)\frac{\partial \langle U_i \rangle}{\partial x_j}\right]}_{\text{(i)}} - \underbrace{C_{\varepsilon 2}\frac{\varepsilon^2}{k}}_{\text{(ii)}}. \tag{2.17}$$

C_μ, σ_k, σ_ε, $C_{\varepsilon 1}$ and $C_{\varepsilon 2}$ are five closure coefficients derived empirically. These closure coefficients are assumed to be universal, however they can be different from one flow to another.
The realizable k-ε model implies a constraint on the predicted Reynolds stress tensor to ensure that the normal stress value can never have a negative value by expressing the closure coefficient C_μ as function of of mean flow and turbulence properties [10]. Furthermore, realizable k-ε involves a modification in the production term (i) of turbulent dissipation energy rate equation which makes it more capable to predict the spreading rate for axisymmetric jets as well as for planar jets, making this model more suitable for flows with large strain rate like flows with strong streamline curvature and rotation [7].

2.2.1.2 The SST $k-\omega$ model

Another way to quantify the turbulent length scale is to use the specific turbulent energy dissipation rate $\omega \propto \varepsilon/k$, which leads to the standard $k-\omega$ model. One of the advantages of this model over the $k-\varepsilon$ model is that the $k-\omega$ model can perform in regions with low turbulence when k and ε approach zero (e.g., near the wall). This cause a problem since k and ε must approach zero at a correct rate as the dissipation term (ii) in Eq. (2.17) includes ε^2/k [7].

The modeled k equation is written as,

$$\frac{\partial k}{\partial t} + \langle U_i \rangle \frac{\partial k}{\partial x_i} = \frac{\partial}{\partial x_i}\Big[\Big(\nu + \frac{\nu_t}{\sigma_k}\Big)\frac{\partial k}{\partial x_i}\Big] + \nu_t\left[\left(\frac{\partial \langle U_i \rangle}{\partial x_j} + \frac{\partial \langle U_j \rangle}{\partial x_i}\right)\frac{\partial \langle U_i \rangle}{\partial x_j}\right] - \beta k\omega, \quad (2.18)$$

and the modeled w equation is

$$\frac{\partial \omega}{\partial t} + \langle U_i \rangle \frac{\partial \omega}{\partial x_i} = \frac{\partial}{\partial x_i}\Big[\Big(\nu + \frac{\nu_t}{\sigma_\omega}\Big)\frac{\partial \omega}{\partial x_i}\Big] + \frac{\omega}{k} C_{\omega 1}\nu_t\left(\frac{\partial \langle U_i \rangle}{\partial x_j} + \frac{\partial \langle U_j \rangle}{\partial x_i}\right)\frac{\partial \langle U_i \rangle}{\partial x_j} - C_{\omega 2}\omega^2, \quad (2.19)$$

and turbulent viscosity can be calculated from

$$\nu_t = \frac{k}{\omega}. \quad (2.20)$$

Similar to $k-\varepsilon$ model, the values β, $C_{\omega 1}$, $C_{\omega 2}$, σ_k and σ_ω are empirical model constants. For boundary layers with adverse pressure gradient, $k-\omega$ model is claimed to have better prediction to the flow. For further information about $k-\omega$ model, the reader is referred to [11].
The Shear Stress Transport (SST) model combines both $k-\varepsilon$ and $k-\omega$ by using a blending function as suggested by Menter [12]. This blending function applies $k-\omega$ model at the near-wall region and $k-\varepsilon$ at the free stream. This model is extensively used in complex turbulent flows like swirling jets and streamline curvatures.

2.2.2 Boundary layer

At a solid wall of any fluid flow, the relative velocity between the fluid and wall is zero due to the wall friction. This leads to a near-wall region where the fluid velocity increases rapidly from zero to the mean fluid velocity. This region is called the boundary layer. To capture the rapid variation of the flow variables in this region, one either applies a fine computational grid near the wall to fully resolve the flow in the region, or uses empirical wall functions to obtain the turbulent quantities at the first grid point far from the wall.
For a turbulent flow, boundary layer can be divided into an outer region where the velocity of the fluid is equal to the mean flow velocity and to an inner region where the velocity of fluid increases rapidly from zero to the mean flow velocity. The inner region is divided into sub-layers based on the magnitude of the turbulent and viscous

parts of the total shear stress, τ_{xy} ,

$$\tau_{xy} = \mu\Big(\frac{\partial\langle U_x\rangle}{\partial y} + \frac{\partial\langle U_y\rangle}{\partial x}\Big) - \rho\langle u'_x u'_y\rangle. \tag{2.21}$$

Near the wall, at the viscous sub-layer, the viscous stress is dominant and molecules viscosity plays a dominant role in momentum transfer and the effective turbulence perpendicular to the wall is almost equal to zero. Further away from the wall, viscous and turbulent stresses are equally effective in momentum transfer. This region can be considered to be a transition region for the flow from laminar flow to turbulent flow and known as buffer sub-layer. At a larger distance from the wall, the turbulent stresses become dominant and viscous effects are negligible. Sub-layers positions are shown in Fig. 2.1.

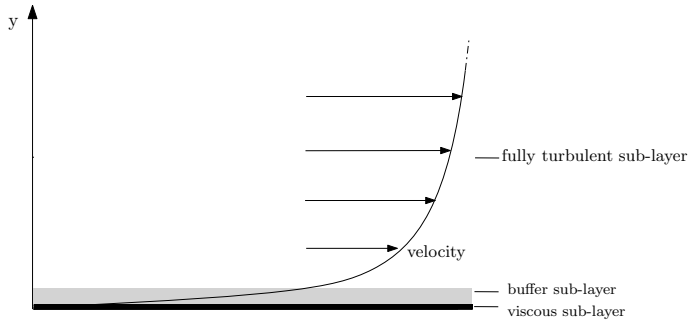

Figure 2.1: Sub-layers at inner region.

The physical extent of these sub-layers are commonly expressed by non-dimensional wall distance y^+ which is defined in terms of wall variables as

$$y^+ = y/l_* = yu_*/\nu, \tag{2.22}$$

where y is the normal distance away from the wall and l_* is the flow characteristic wall length and u_* is the wall friction velocity and defined as

$$u_* = \sqrt{\tau_w/\rho}, \tag{2.23}$$

where τ_w is the viscous shear stress at the wall

$$\tau_w = \rho\nu\frac{\partial\langle U_x\rangle}{\partial y}\bigg|_{y=0}. \tag{2.24}$$

Inner region sub-layers are experimentally classified in terms of y^+ as the following [7]

i. Viscous sub-layer $0<y^+<5$
ii. Buffer sub-layer $5<y^+<30$
iii. Fully-turbulent sub-layer $30<y^+<400$

As discussed before, the velocity gradient at the inner region is relatively high compared to the mean flow gradient. In order to capture this large change in flow

properties near the wall, high mesh resolution is required for solving the governing equations accurately. This approach is commonly known as low Reynolds number approach where no modeling beyond the assumption of laminar flow is necessary in the wall cells. This method corresponds to wall treatment method at Star-CCM+ named as *low y^+ wall formulation*. As a consequence of using a very dense mesh near the wall, this method could be highly demanding in terms of computational resources and time. Hence, another approach could be followed where a wall function is used to bridge the near-wall region. This method is commonly known as high Reynolds number approach or wall function and corresponds to wall treatment method at Star-CCM+ named as *high y^+ wall formulation*. Wall functions are semi-empirical rules used to avoid having dense mesh near the wall region and also may be needed since some particular turbulence models like standard $k-\varepsilon$ are not valid in the viscosity-affected near-wall region. The basic idea of wall function is to apply boundary conditions at a point some distance away from the wall where the turbulence models are not solved at this distance. Wall function is commonly applied at the inner region boundary layer which means that the first cell near the wall should have a perpendicular distance that achieves $y^+ > 400$, while for using low y^+ wall formulation the first cell should have a very small perpendicular distance that achieve $y^+ \approx 1$. Star-CCM+ provides an additional wall treatment formulation called *Two-layer all y^+ wall formulation* [10] that uses a blending function in terms of the wall-distance to use both low and high wall treatments.

2.3 Numerical methods for CFD

This section briefly discusses the common numerical methods used to mathematically solve the flow governing equations in CFD simulations.
It is not generally possible to solve flow transport equations analytically since they are non-linear equations and contain both spatial and temporal derivatives. For simplification, general transport equation for arbitrary variable ϕ in conservation form is introduced as the following:

$$\underbrace{\rho\frac{\partial\phi}{\partial t}}_{\text{(i)}}+\underbrace{\rho\frac{\partial(u_j\phi)}{\partial x_j}}_{\text{(ii)}}=\underbrace{\frac{\partial}{\partial x_j}\left(\Gamma\frac{\partial\phi}{\partial x_j}\right)}_{\text{(iii)}}+S_\phi, \tag{2.25}$$

where Γ is the diffusion coefficient and S_ϕ is a source term that depends on the variable ϕ. Terms (i), (ii) and (iii) are known as transient, convection and diffusion terms respectively.

2.3.1 Finite volume method

Finite volume method divides the computational domain into a finite number of small cells and by integrating the transport equations over a control volume (cell) and by applying Guass' theorem, the partial differential equations (PDE) can be

re-written as algebraic equations and solved numerically in an easier way. The information about the flow is solved and stored at the center of the cell. The cost of discretizing the computational domain into small volume cells is the introduction of error in the solution [7].

If finite volume method and Gauss' theorem is to be applied on the convection term in the general transport equation (2.25) it gives the following

$$\int_{c.v} \frac{\partial \rho u_j \phi}{\partial x_j} dV = \int_{c.s} \rho u_j n_j \phi dA, \tag{2.26}$$

where n refers to a normal vector pointing outwards from the surface of the cell dA. For a structured 3D mesh, Eq. (2.26) can be written as

$$-\rho\Big[(Au_x\phi)_w - (Au_x\phi)_e + (Au_y\phi)_s - (Au_y\phi)_n + (Au_z\phi)_t - (Au_z\phi)_b\Big], \tag{2.27}$$

where indices w,e,s,n,t, and b refer to west, east, south, north, top and bottom faces of the control volume respectively. For simplification, Eq. (2.27) can be represented as 1D control volume in the direction of x-axis, which means that integration from the west to east faces is only accounted for. The next step is to estimate the value of ϕ at the faces. This can be done by using several methods which each have their own advantages and disadvantages based on the nature of the flow. In this problem, central-differencing discretization scheme is followed using linear interpolation from the values in the neighboring cells. Based on Fig. 2.2 value at the cell faces are obtained as the following.

$$\phi_w = \frac{\phi_W + \phi_P}{2}, \tag{2.28}$$

$$\phi_e = \frac{\phi_P + \phi_E}{2}. \tag{2.29}$$

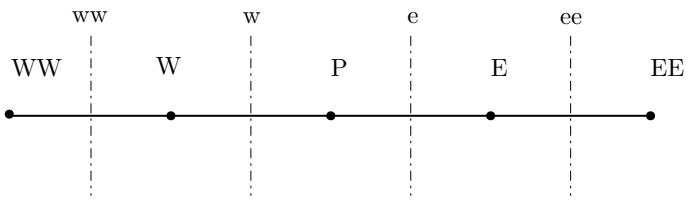

Figure 2.2: One dimensional domain describing neighboring cells and cell faces.

As mentioned earlier, flow information is solved and stored at the center of the cell. By neglecting transient, source, and diffusion terms in general transport equation, Eq. (2.25) can be written as

$$\rho u_x\Big[(\frac{\phi_P + \phi_E}{2}) - (\frac{\phi_W + \phi_P}{2})\Big] = 0. \tag{2.30}$$

N number of equation is solved for N number of cells with three unknown variables; ϕ_W, ϕ_E and ϕ_P for each equation. However, the value of ϕ_E in the equation of cell number 3 is the value of ϕ_P in the equation of cell number 4, concluding that the total number of the unknown variables is N plus two additional variables for the furthest eastern and western faces.

In order to solve these equations, two imaginary cells can be added outside of the computational domain to estimate the values of faces at the boundaries of the computational domain.

2.3.2 Spatial discretization schemes

As discussed in the previous section, central-differencing scheme is used to estimate and evaluate the value of flow variables at the faces of the cell. This method simply takes the linear average of the adjacent cells disregarding the effect of flow direction and magnitude. Upwind schemes are usually used in applications with high flow rate where the convection transport become more dominant to avoid the solution from diverging [7].

2.3.2.1 First-order upwind

Upwind schemes add to the discretization process a very important property which is called *transportiveness* [7] where the numerical scheme takes the flow direction into account by increasing the effect of the upstream cells of the flow in the computational domain. This is done by letting the value of the phase between two cells equal to the nearest upstream cell as the following;

$$\begin{aligned} \phi_w &= \phi_W, \\ \phi_e &= \phi_P. \end{aligned} \tag{2.31}$$

2.3.2.2 Second-order upwind

To increase discretization scheme accuracy and avoid *numerical diffusion* [7], second-order upwind takes information from two upstream cells instead of one by assuming that the gradient between eastern and present cell is equal to the gradient between present and west cell, which gives for equidistant grid the following expression.

$$\phi_w = 1.5\phi_W - 0.5\phi_{WW}. \tag{2.32}$$

The main drawback of this method is that it is *unbounded*, which means that the value of the estimated phase does not necessarily lay between the values used to calculate it. This could cause several numerical instabilities and lead to divergence of the solution. Several developments to second-order schemes are applied to overcome this problem.

2.3.3 Temporal discretization scheme

For time-dependant problems, the transient term in Eq. (2.25) can no longer be ignored and the whole transport equation is integrated in time from an initial time value (t) to ($t + \Delta t$). Similar to the spatial discretization, different schemes can be applied to evaluate the temporal gradient of certain entity ϕ.
Variables are calculated between time t and Δt. Different discretization schemes are categorized depending on the time boundary used to evaluate the result. The first is

called *explicit discretization* scheme, where the value of ϕ at the previous time step is used explicitly to calculate the new value of ϕ. This method requires great attention when picking the value of the time step as it should be small enough to capture the change of the variables within the required spatial frame which can make it computationally expensive. The second method is called *fully implicit discretization* scheme. This method does not use the value in the previous time step but instead uses the value at the later time step which makes it unconditionally bounded. Unlike explicit scheme, this method requires inner sub-iterations within each time step as the value of the variables is not explicitly known at later time step. The number of sub-iteration should be enough to achieve convergence before moving to the next time step.

2.3.4 Measuring convergence

There are many methods to judge whether the solution is converged or not. The most common one is to compare the numerical solution from one iteration to another and set a small threshold for convergence. Another way is to check the global convergence of the whole domain by monitoring a certain entity at the inlet and the outlet of the computational domain, in the absence of any source of this entity, the difference between these two values should be fairly small to achieve convergence.

2.4 Fan modelling

In this project, the multiple reference approach is followed to model the fan. In this approach the computational domain is divided into two zones, stationary and rotating, with interface surfaces separating them. The rotational movement of the fan rotor is commonly simulated in two different methods. The first method is called moving reference frame (MRF). This method is used in this project to offer an initial evaluation of the quality of the mesh and the accuracy of the turbulence models. The second method is the sliding mesh approach, where the mesh in the rotation zone is moving with the rotor. Compared to the MRF, this method is more computationally expensive but able to provide prediction of the unsteady flow field of the rotating fan. Therefore the acoustic source in this study is constructed from the unsteady flow variables obtained using the sliding mesh approach.

2.4.1 Moving reference frame

The MRF method is typically used to simulate rigid body rotation without the need to move the mesh. Fig. 2.3 describes the coordinate transformation from stationary frame to rotating frame. The rotating zone is solved in the rotating frame and stationary zone solved in the stationary frame and both of the zones have a stationary mesh. The main advantage of this approach is the ability to convert the unsteady problem to a steady one and represent the time-averaged properties of the flow, decreasing the computational demand significantly. The equations of motion can be solved either in absolute velocity, u, or relative velocity, u_r, formulation. The

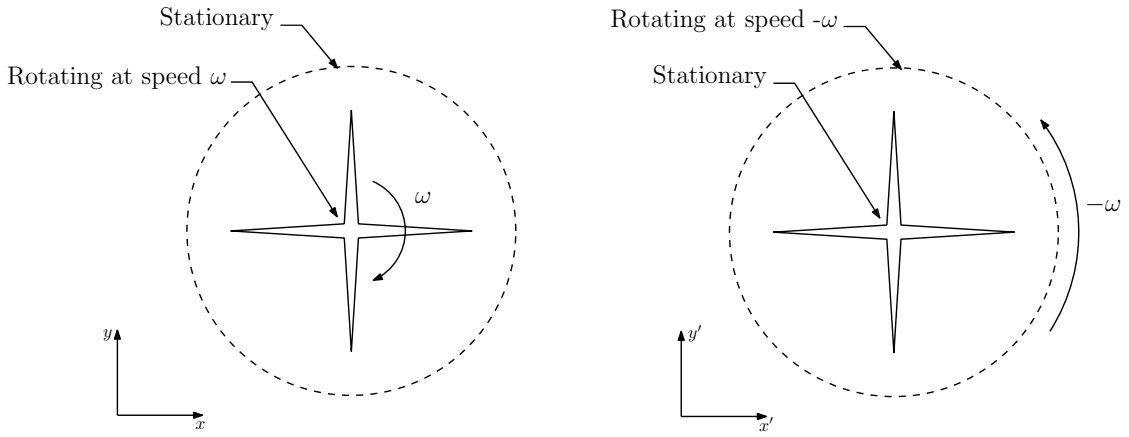

(a) Stationery reference frame. (b) Moving reference frame.

Figure 2.3: Comparison between moving and stationery reference frames.

relation between both velocities can be written as

$$\vec{u_r} = \vec{u} - (\vec{\omega} \times \vec{r}), \tag{2.33}$$

where $\vec{\omega}$ is the angular velocity of the rotating reference frame and $\vec{r}$ is the position vector in the rotating frame. For solving equations of motion in rotating reference frame, governing equations can be written in terms of relative velocity as

$$\frac{\partial \rho}{\partial t} + \frac{\partial \rho \vec{u_{r,i}}}{\partial x_i} = S_m, \tag{2.34}$$

$$\frac{\partial \rho \vec{u_{r,i}}}{\partial t} + \rho \frac{\partial \vec{u_{r,i}} \vec{u_{r,j}}}{\partial x_j} + \rho(2\vec{\omega} \times \vec{u_{r,i}} + \vec{\omega} \times \vec{\omega} \times \vec{r}) = -\frac{\partial p}{\partial x_i} + \frac{\partial \tau_{ij}}{\partial x_j} + \vec{f_i}. \tag{2.35}$$

Two additional terms appear in Eq. (2.35) that represent Coriolis acceleration and centripetal acceleration that arose from the transformation of coordinates from stationary frame to a rotating one. MRF is also known as frozen rotor approach as it is analogous to freezing the motion of a moving part in a certain position and monitoring the instantaneous flow field with the rotor in that position [13]. At the interface between regions with different reference frames, local variables are transformed from one frame to another on a cell-by-cell basis and then the transformed variables are used to calculate the fluxes at the interface of the adjacent region [10]

2.5 Aeroacoustics

Aeroacoustics is a branch of fluid mechanics that deals with sound generated from aerodynamics. Noise generated by flow is basically due to fluctuation in flow properties that can be created through different mechanics, such as turbulent motions, fluctuations in external forces or heat sources.
The energy associated with the sound generated by flow is generally small compared to the total energy of the flow, so it is difficult to predict the aeroacoustic noise by directly solving the full fluid-mechanics equations. Many acoustic analogies therefore

have been formulated to separate the "sound" from the main flow fluctuations. This section gives a brief description of the general acoustic wave equation and the acoustic analogy related to this project.

2.5.1 Acoustic wave equation

The perception of sound to the human ear is mainly through fluctuating pressure $\grave{p}$ which is also known as acoustic pressure. In aeroacoustics, sound is generated from the small fluctuations in flow variables that can be presented as perturbation from reference state of density ρ_o, pressure p_o, and velocity u_{io},

$$\grave{p} = p - p_o, \quad \grave{\rho} = \rho - \rho_o, \quad \grave{u}_i = u_i - u_{io}. \tag{2.36}$$

The propagation of the small fluctuations can usually be described by certain linearized fluid-mechanics equations, including the wave equation. The classic acoustic wave equation is derived by assuming that the propagation of sound is an inviscid, adiabatic and linear process. Under such an assumption, the propagation of "sound" in quiescent fluid, u_o=0, is described by the following equations of motions

$$\frac{\partial \grave{\rho}}{\partial t} + \rho_o \frac{\partial \grave{u}_i}{\partial x_i} = Q_m, \tag{2.37}$$

$$\rho_o \frac{\partial \grave{u}_i}{\partial t} + \frac{\partial p}{\partial x_i} = f_i, \tag{2.38}$$

$$\grave{p} = c_o^2 \grave{\rho}. \tag{2.39}$$

Subtracting the divergence of Eq.(2.38) from the time derivative of Eq.(2.37) yields the following non-homogeneous acoustic wave equation

$$\frac{1}{c_o^2}\frac{\partial^2 \grave{p}}{\partial t^2} - \frac{\partial \grave{p}}{\partial x_i^2} = -\frac{\partial f_i}{\partial x_i} + \frac{\partial Q_m}{\partial t}. \tag{2.40}$$

The first and second term at the right-hand side of Eq.(2.40) represents sound production from unsteady external force field and mass fluctuations, respectively [14]. These two sources, however, are not the same as the aerodynamic sources as in the Lighthill's analogy that is introduced in the next section.

2.5.2 Lighthill's analogy

The idea behind the Lighthill's analogy is to connect acoustics and fluid mechanics by formulating a non-homogeneous "wave equation" that models the acoustic source through fluid governing equations. The main concept of the analogy is to decouple the noise generation and propagation. In the analogy, the non-homogeneous "wave equation" is derived by subtracting the divergence of the momentum equation (2.2) with $f = 0$ from the time derivative of the continuity equation (2.1) with $Q_m = 0$, and subtracting the term $c_o^2 \partial^2 \grave{\rho}/\partial x_i^2$ from both sides. By using the definition of flow perturbations in Eq. (2.36), the "wave equation" reads

$$\frac{\partial^2 \grave{\rho}}{\partial t^2} - c_o^2 \frac{\partial^2 \grave{\rho}}{\partial x_i^2} = \frac{\partial^2 T_{ij}}{\partial x_i x_j}, \tag{2.41}$$

in which Lighthill's stress tensor T_{ij} is defined as

$$T_{ij} = \rho u_i u_j - \tau_{ij} + (\grave{p} - c_o^2 \grave{\rho})\delta_{ij}. \tag{2.42}$$

The first term at the right-hand side of Eq. (2.42) is the Reynolds stress that accounts for the nonlinear convection of momentum; the second term is the viscous stress which is induced by molecular transport of momentum; the last term describes complex effects due to convection of entropy non-uniformities [15].
In this project, the Lighthill's analogy is solved with Actran [16] in the frequency domain by adopting the variational formulation of the analogy derived by A Oberai et al. [17]

$$-\int_\Omega \frac{\omega^2}{\rho_o c^2}\psi\delta\psi\partial\Omega - \int_\Omega \frac{1}{\rho_o}\frac{\partial\psi}{\partial x_i}\frac{\partial\delta\psi}{\partial x_i}\partial\Omega = \int_\Omega \frac{\mathrm{i}}{\rho_o\omega}\frac{\partial\delta\psi}{\partial x_i}\frac{\partial T_{ij}}{\partial x_j}\partial\Omega - \int_\Gamma \frac{\delta\psi}{\rho_o}\mathcal{F}(\rho u_i n_i)\partial\Gamma, \tag{2.43}$$

where $\psi = \mathrm{i}\grave{\rho}c_0^2/\omega$ is the velocity potential, $\delta\psi$ is a test function (the variation), Ω is the volumetric part of the computational domain, Γ is the boundary of the computational domain, and $\mathcal{F}$ indicates the Fourier transform. The variable ω in Eq. (2.43) denotes the angular frequency.
The first term at the right-hand side of Eq. (2.43) represents the contribution of the volumetric aeroacoustic source, whereas the second term represents the contribution of the surface source and described by Actran as Lighthill's surface density. It should be noted that, in the calculation of the volumetric source Actran approximates the Lighthill's stress tensor as [16]

$$T_{ij} \approx \rho u_i u_j, \tag{2.44}$$

which is valid for isentropic process and low-Mach-number flows [18].
One can compare the above variational formulation with the Curle's analogy [19]. The differential form of the latter reads [20]

$$\left(\frac{1}{c_0^2}\frac{\partial^2}{\partial t^2} - \frac{\partial^2}{\partial x_i^2}\right)\left(Hc_0^2\grave{\rho}\right) = \underbrace{\frac{\partial^2\left(HT_{ij}\right)}{\partial x_i\partial x_j}}_{\text{Volumetric quadrupole}} + \underbrace{\frac{\partial}{\partial t}\left(\rho u_i\frac{\partial H}{\partial x_i}\right)}_{\text{Surface monopole}} - \underbrace{\frac{\partial}{\partial x_i}\left[\left(\rho u_i u_j + \grave{p}\delta_{ij} - \tau_{ij}\right)\frac{\partial H}{\partial x_j}\right]}_{\text{Surface dipole}}. \tag{2.45}$$

where H is the Heaviside unit function defined by

$$H = \begin{cases} 1, & \text{for } \boldsymbol{x} \text{ in } \Omega, \\ 0, & \text{otherwise.} \end{cases} \tag{2.46}$$

It can be shown that $\partial H/\partial x_i$ is nonzero only at the surface of the computational domain Γ. It is worth noting that the integral surface can be either rigid walls or permeable surfaces located within the flow. In this study, a permeable surface is

used as the integral surface. By using Eq. (2.42), Eq. (2.45) can be reformulated as

$$\begin{aligned}\frac{1}{c_0^2}\frac{\partial^2\left(Hc_0^2\grave{\rho}\right)}{\partial t^2}-\frac{\partial}{\partial x_i}\left(H\frac{\partial c_0^2\grave{\rho}}{\partial x_i}\right)&=\frac{\partial^2\left(HT_{ij}\right)}{\partial x_i\partial x_j}+\frac{\partial}{\partial t}\left(\rho u_i\frac{\partial H}{\partial x_i}\right)\\&\quad-\frac{\partial}{\partial x_i}\left\{\left[\rho u_iu_j+\left(\grave{p}-c_0^2\grave{\rho}\right)\delta_{ij}-\tau_{ij}\right]\frac{\partial H}{\partial x_j}\right\}\\&=\frac{\partial}{\partial x_i}\left(H\frac{\partial T_{ij}}{\partial x_j}\right)+\frac{\partial}{\partial t}\left(\rho u_i\frac{\partial H}{\partial x_i}\right).\end{aligned}\tag{2.47}$$

Then, the variational formulation Eq. (2.43) can be derived by multiplying the Fourier transform of Eq. (2.47) by the variation and integrating over Ω. It can be seen from the reformuated Curle's analogy Eq. (2.45) and the variational formulation Eq. (2.43), that the dipole source in the original Curle's analogy is "merged" into the modified quadrupole source. This indicates that the dipole contribution, which may dominate over the quadrupole and monopole at low Mach numbers in the presence of rigid surfaces, is accounted for by the variational formulation in the form of reflection of quadrupole-generated sound at the boundaries.
In some cases, the local non-linear turbulent stress may be relatively weak and the monopole may dominate over the quadrupole (such as the case treated in our study where the acoustic domain positioned at the suction side of the fan experiences relatively weak turbulent stresses). In such cases one may only keep the monopole contribution in the variational formulation; this is then equivalent to the Kirchhoff-Helmholtz formulation, the differential form of which reads [21]

$$\left(\frac{1}{c_0^2}\frac{\partial^2}{\partial t^2}-\frac{\partial^2}{\partial x_i^2}\right)\left(Hc_0^2\grave{\rho}\right)=-\frac{\partial}{\partial x_i}\left[\grave{p}\frac{\partial H}{\partial x_i}\right]+\frac{\partial}{\partial t}\left(\rho u_i\frac{\partial H}{\partial x_i}\right).\tag{2.48}$$

Applying the variational formulation to Eq. (2.48), one can show that only the "monopole"-related term $\partial\left(\rho u_i\partial H/\partial x_i\right)\partial t$ remains at the right-hand side of the final equation. Because all the flow quantities involved in the Kirchhoff-Helmholtz formulation must satisfy the wave equation, using only the contribution of the surface source in Eq. (2.43) implicitly requires that the flow quantities on the source surface (either permeable or impermeable) should be able to be treated as those that satisfy the linear, inviscid and adiabatic flow equations.

3

Simulation setup

3.1 CFD simulation

3.1.1 Geometry

The first step for setting up the CFD simulation is to have a simple geometrical representation of the computational domain in the form of a computer-aided drawing (CAD). The CAD file used in this project is supplied upon request by Zenger et al. [2] and imported to the pre-processing software ANSA for further reprocessing. The axial fan rotor consists of 9 blades that have a hub radius ($r_{\text{hub}} = 0.124m$) and a tip radius ($r_{\text{tip}} = 0.247m$). The fan is installed in a short duct with a radius ($r_{\text{duct}} = 0.25m$. It is necessary to clean the CAD file and prepare the geometry surface before performing surface meshing. The cleaning process focused on removing unnecessary parts that have no effect on the measured flow properties. Unwanted sharp edges and holes are also removed to obtain more robust surface mesh and reduce the number of computational cells as shown in Fig. 3.1 and Fig. 3.2.

For rotating turbomachinary applications, it is common to divide the computational domain into rotating and stationary parts. The computational domain present at hand is divided into three separate parts; inlet and outlet are the stationery parts and the fan region in the middle is the rotating part. The rotating part is separated from the other stationary parts by two conformal interface surfaces. Inlet and outlet volume domains are defined in shape of two separate cuboids with cross section similar to the inlet chamber of the measurement facility as seen in Fig. 3.3. The next step is to define all of the available geometrical parts and apply high resolution triangular surface mesh. This step is essential in order to find out and fix irregular surfaces that could result to a bad volume mesh, especially around sharp edges and high surface curvatures.

3.1.2 Volume meshing

After preparing the geometry and producing the surface mesh, the file is imported to the main CFD analysis software Star-CCM+ as a surface mesh file in ".nas" format. Star-CCM+ has several meshing models that are used in this project such as, *surface remesher, prism layer and the core volume mesher*. Surface remehser improves the overall quality of the surface and optimizes it for the volume mesher in addition to supporting the subsurface generator when prism layer mesher is selected [10].

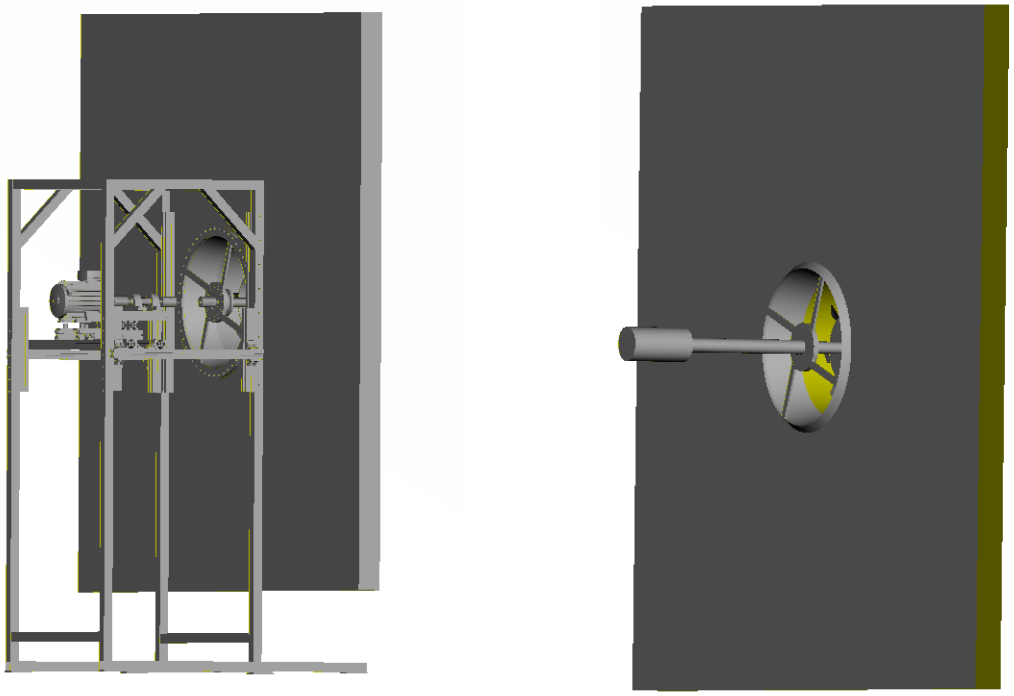

(a) Original geometry. (b) Cleaned geometry.

Figure 3.1: Fan pressure side, before and after cleaning.

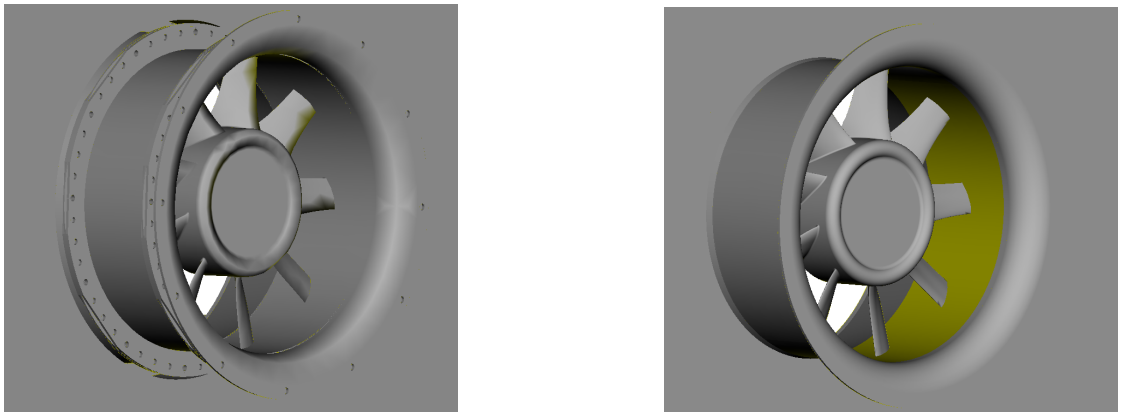

(a) Original geometry. (b) Cleaned geometry.

Figure 3.2: Fan suction side, before and after cleaning.

3.1.2.1 Prism layer

The prism layer mesher is used to improve the accuracy of resolving boundary flows near the walls. As discussed in Sec. 2.2.2, there are two common approaches for resolving boundary layer flow, choosing either of them depends on many other specifications such as, turbulence model selected, shape of the physical domain simulated and the available computational resources. A small boundary layer test (Appendix A) is executed to compare different y^+ wall treatments for different turbulence models in STAR CCM+. For the realizable $k-\varepsilon$ model, the study shows that the low y^+

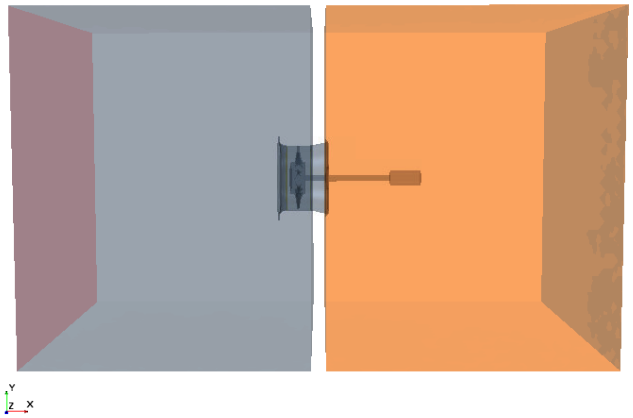

Figure 3.3: CFD computational domain and the coordinate system followed

mesh in combination with all y^+ wall treatment and the medium y^+ mesh in combination with high y^+ wall treatment gave accurate boundary flow results, while for using medium y^+ mesh in combination with all y^+ wall treatment, less accurate results are obtained. Since it is difficult to know all of y^+ values in the computational domain, low y^+ mesh with all y^+ wall treatment is chosen for the simulation. Prism layer mesher produces orthogonal prismatic cells with high aspect ratio near the surface walls to provide better cross-stream resolution without effecting the streamwise resolution [10]. Several factors are considered when setting up the prism layer specifications to fully take advantage of the mesher tool and avoid high discretization errors.

- Smooth cell size transition between prism layers region and the core volume mesh region. The thickness of the first prism layer chosen to achieve $y^+ \approx 1$ is 0.0075 mm. To have a good transition along the prism layer region, 22 prism layers are chosen with a total thickness of 0.008 m and stretching factor of 1.3
- Control prism layer total thickness when boundary surfaces are close to each other as shown in Fig. 3.4(a)
- Set a specific aspect ratio between the thickness and the width of last prism cell layer near the core volume mesh. This improves the transition from the prism layer to the core mesh especially around sharp edges and curvatures as seen in Fig. 3.4(b)

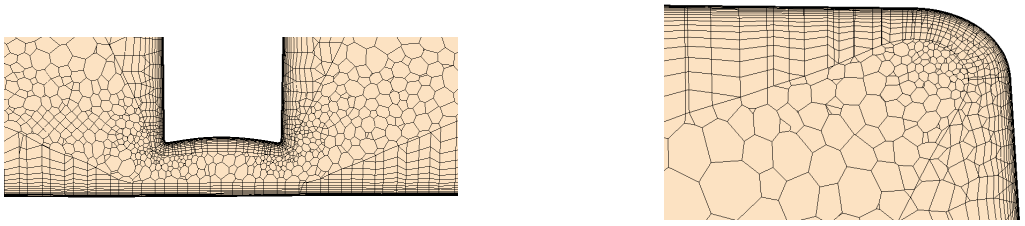

(a) Close boundary surfaces.

(b) Near wall adjusted aspect ratio.

Figure 3.4: Prism layer specific properties.

Fig. 3.5 shows y^+ values at a rotor blade where the highest possible flow velocity values are at the tip, trailing edge and leading edge of the blades and have $y^+ \approx 1$

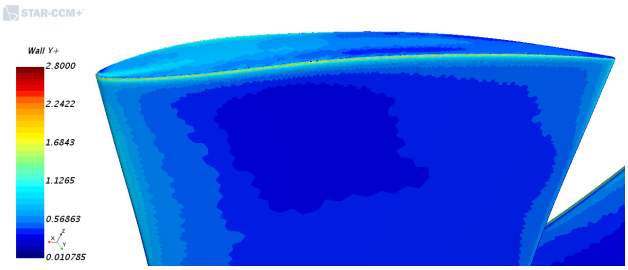

Figure 3.5: y^+ contour at rotor blades.

3.1.2.2 Core volume mesh

Polyhedral and trimmed volume mesh models are used for the steady and unsteady simulations to compare their efficiency when it comes to accuracy, cell count, computational demand and the time needed to formulate the mesh and reach a converged solution. Trimmed cell mesher main advantage is the short time required for building the mesh and the production of more structured cells compared to polyhedral mesh as shown in Fig. 3.6. Although the trimmed model produces higher cell count, the number of cell faces is much less than the polyhedral mesh which results in faster iteration process for same computational resources. For steady simulation, the two mesh models have taken nearly the same number of iterations to reach convergence;however, results showed that polyhedral mesh gave more accurate results as it is discussed in Sec. 4.2.2. Tab. 3.1 shows a comparison between the two mesh models properties.

Mesh structure	Polyhedral mesh	Trimmed mesh
Cell count	20 M	24 M
No. of faces	92.5 M	70 M
No. of iterations for convergence	2800	2500

Table 3.1: Mesh models properties.

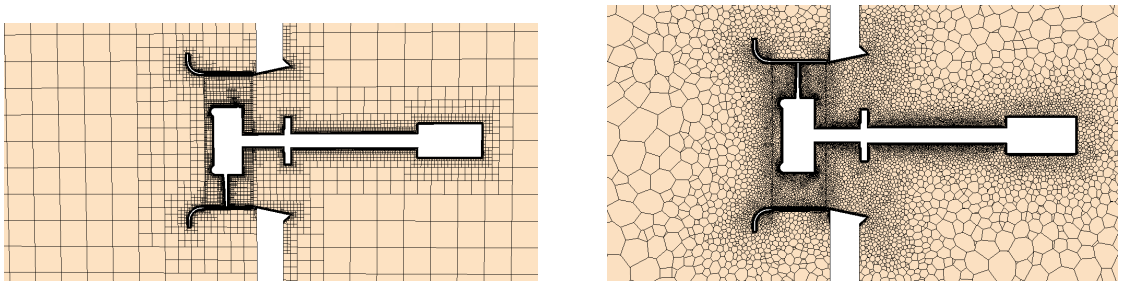

(a) Trimmed mesh.

(b) Polyhedral mesh.

Figure 3.6: Mesh structure cross section.

The mesh is refined at regions with high velocity gradients at trailing edges, leading edges and tips of the rotor blades, in addition to the wake region after the rotor. Prism layer mesher is not applied at the wall sides of the inlet and outlet regions, since the velocity at this regions are very low and does not affect the flow study.

3.1.3 Boundary conditions

Before generating surface and volume meshes, boundary conditions are assigned to different parts of the computational domain to represent the physical surroundings of the experimental facility. The rectified flow at the inlet is represented by uniform inlet velocity assigned to the far left face of the inlet region with value of 0.308 m/s which corresponds to the design volumetric flow rate 1.4 kg/m^3. Rest of the faces are treated as hard wall with no-slip boundary condition as well as the walls between inlet and outlet regions and the whole rotor and fan frame geometry. For the outlet region, the free outflow from the test chamber to the atmospheric ambient is represented by assigning the surrounding faces to pressure outlet and setting it to the atmospheric pressure value.
Moving reference frame is applied to the fan region in the steady simulation to simulate the rotation effect of the rotor, while sliding mesh approach is applied in the unsteady simulation to obtain more accurate results. The new reference is created by setting axis of rotation coordinates and the rotating speed of the rotor. The whole rotating region is assigned to the new reference frame except for the outer region which represents the stationary duct. The rotating shaft that lies in the outlet region is also assigned to the new reference frame. For sliding mesh approach, a rotation motion for the mesh vertices is specified in the unsteady simulation by setting axis of rotation coordinates and the rotation speed. The rotation motion property is assigned to the same geometrical parts assigned in the steady simulation.

3.1.4 Physics

This section discusses the main physical models and mathematical formulations that are used in the simulation to represent the flow.

Incompressible with constant density model flow is chosen, since the highest possible flow velocity at the tip of the rotor blade had a Mach number of 0.123. Ambient air properties are assigned for the medium flow with a density of 0.187 kg/m^3 and dynamic viscosity of $1.85\times10^{-}5$ Pa.s.
Initially, The realizable $k-\varepsilon$ and the $k-\omega$ (SST) turbulence models are used for the steady simulation to evaluate model accuracy. The realizable $k-\varepsilon$ with two-layer all y^+ treatment is used as the main turbulence model for further simulations based on the results discussed in Sec. 4.2.2. Segregated flow solver is chosen for solving flow variables including pressure and velocity, more information about the flow solvers used in Star-CCM+ are discussed in Sec. 3.1.5. Tab. 3.2 shows the physics models and settings used in steady and unsteady simulations.

Space	Three Dimensional
Time	Steady / Implicit Unsteady
Material	Gas
Flow solver	Segregated flow
Equation of State	Constant Density
Viscous Regime	Turbulent
Turbulence model	RANS (Realizable K-Epsilon Two-layer / SST K-Omega)
Wall treatment	All y^+ wall treatment

Table 3.2: Physics models.

3.1.5 Solver settings

3.1.5.1 Pressure-velocity coupling

In incompressible flow simulations, the four conservation equations (one conservation of mass and three conservation of momentum) consist of four unknown variables (pressure and three velocity components), so the four equations could be directly solved. In doing so, however, numerical issues (such as numerical instability) are commonly encountered. Therefore, iterative process where the mass and momentum equations are decoupled is usually adopted to solve the set of equations. The iterative process starts by guessing initial value for the pressure field and then the velocity components are solved through the momentum equations. Most probably the velocities evaluated do not satisfy the continuity equation, so the pressure is updated by pressure correction factor that depends on the mesh and the flow field. The main idea behind the process is to find a good equation for the pressure correction as a function of mass imbalance. This iterative process is commonly known as the SIMPLE algorithm.

The SIMPLE algorithm is used in this study.

3.1.5.2 Coupled and segregated flow solvers

Star-CCM+ uses coupled and segregated flow solvers to solve the conservation equations of mass and momentum. Coupled flow method solves all the flow variables simultaneously for a certain cell, then moves to the next one. Segregated flow method, on the other hand, solves only one flow variable for all domain cells, then moves to the next flow variable and solves again for all cells. The coupled flow solver is considered more accurate and robust for compressible flows, particularly in the presence of shocks. Segregated flow solver is more convenient to be chosen if incompressible flow is considered. In addition, segregated flow solver uses mush less memory than the coupled flow solver.

Because of the incompressible-flow assumption adopted in our study, the segregated flow solver is chosen here.

3.1.5.3 Discretization schemes and time step

Second order spatial discretization scheme is used in our steady and unsteady simulation. Compared to the first order scheme, the second order scheme is expected to offer more accurate results and help avoid numerical diffusion, as has been discussed in Sec. 2.3.2.
For temporal discretization scheme in unsteady simulation, implicit unsteady scheme is used where each time step consists of inner iterations. The number of inner iterations can be set by monitoring one or more specific quantities against iterations and determining if those quantities are converging within each time step or not.
Compared to the explicit method, the implicit discretization method is featured by allowing the use of large time-steps. Even though, to avoid possible numerical errors related to the rotation of the fan, the time step is chosen to be 1×10^{-4} which corresponds to an angle of rotor rotation that is nearly less than 1°[22].

3.1.6 Measuring points

3.1.6.1 Velocity and wall pressure fluctuations

Following the measurement setup done by Zenger [2], 26 flow measuring points are placed at both the pressure and the suction sides of the rotor to extract the axial velocity profile along the rotor blade; see Fig. 3.7(a). In addition, 15 pressure probes are placed along a line on the fan duct with an equal spacing of 10 mm to extract the unsteady pressure fluctuations; see Fig. 3.7(b).

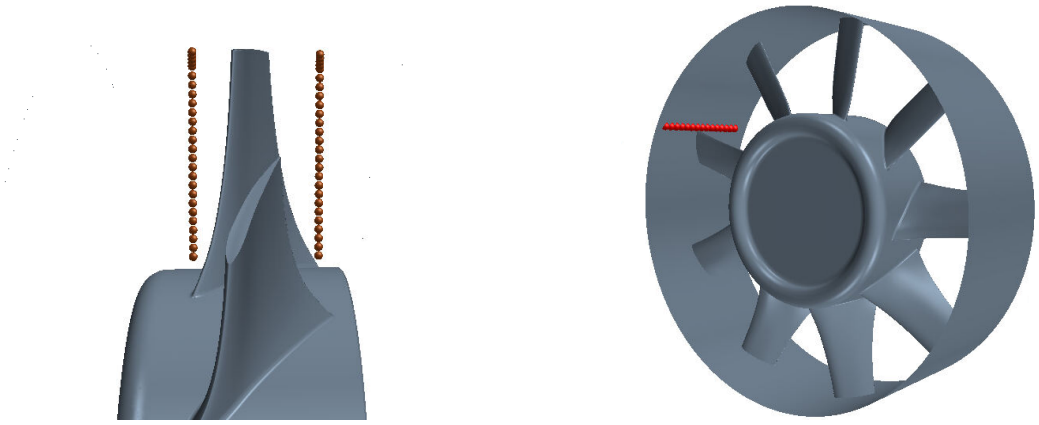

(a) Axial velocity probes.

(b) Wall pressure probes.

Figure 3.7: Flow field measuring points.

3.2 Acoustic simulation

The acoustic field is computed with Actran using the finite element method. In this section, the acoustic simulation setup is discussed, including the surface noise source, the volume mesh, the boundary conditions, and the measuring points.

3.2.1 Surface noise source

After establishing a robust CFD simulation model by verifying the numerical flow results against the experimental results, aeroacoustic source is imported to the acoustic simulation software, Actran, to analyze the aerodynamically generated noise through the Lighthill's analogy. The Actran module, Lighthill surface, is applied to generate surface sources.
As can been see from the Lighthill's analogy, Eq. (2.43), the aeroacoustic source consists of volumetric and surface contributions. In this study we only use the surface contribution to compute the acoustic field because the volumetric contribution is considered relatively weak at the suction side of the fan.
While choosing the surface source location, the initial plan is to extract the velocity surface source at the interface between the inlet and the fan regions; however, it is found that interface flow data extracted from Star-CCM+ are unreadable by Actran. Therefore, the surface source is instead positioned a short distance towards the inlet region on a surface created externally in ANSA; see Fig. 3.8

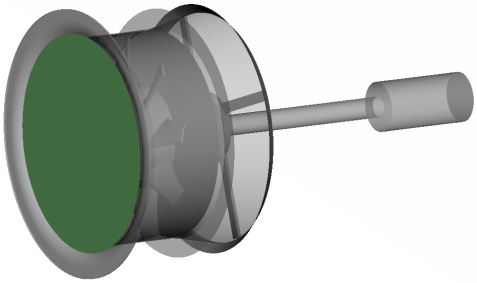

Figure 3.8: New surface source position highlighted in dark green.

Fig. 3.9 shows the difference between the velocity contours in both positions, noticeable overlap between surface cells at the interface position which probably caused the files to be unreadable. The surface source file is then processed in Actran through

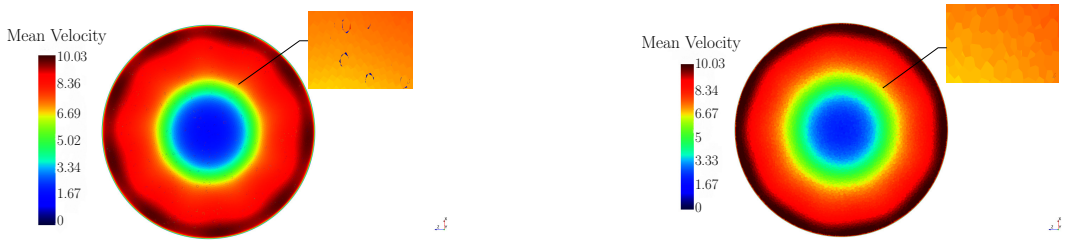

(a) Source surface at the interface position.

(b) Source surface at the new position.

Figure 3.9: Velocity contour of different surface sources.

an inner utility called "iCFD", which computes the aeroacoustic source through the application of Lighthill's analogy and then maps the extracted quantities to the acoustic mesh and finally performs the Fourier transform to the data in order to solve the acoustic equation in the frequency domain. The CFD-extracted quantities

are mapped by integration of aeroacoustic fields over the CFD mesh using the shape function of the acoustic mesh [16].

3.2.2 Volume mesh and boundary conditions

Compared to the CFD mesh, the acoustic volume mesh is applied to the inlet and rotational regions, but not to the outlet region. This is because that the measurement data to be compared are only available at the suction side, so, when the Lighthill's analogy is used, it is unnecessary to study the noise propagation at the pressure side of the fan. The surface and volume mesh are generated by ANSA. The surface mesh consists of nearly 71 thousand triangular cells with the smallest dimension size of 5 mm, while the volume mesh consists of nearly 2.3 million tetrahedral cells. Part of of volume mesh at a cross section of the acoustic domain is shown in Fig. 3.10.

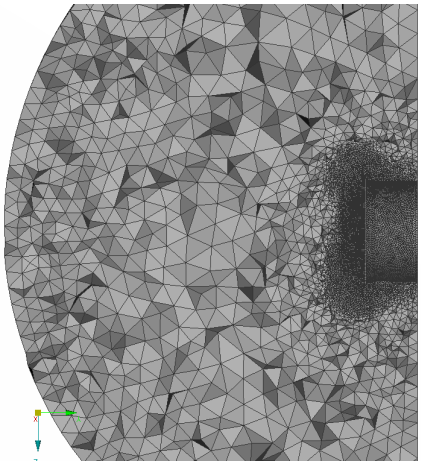

Figure 3.10: Mesh structure cross section.

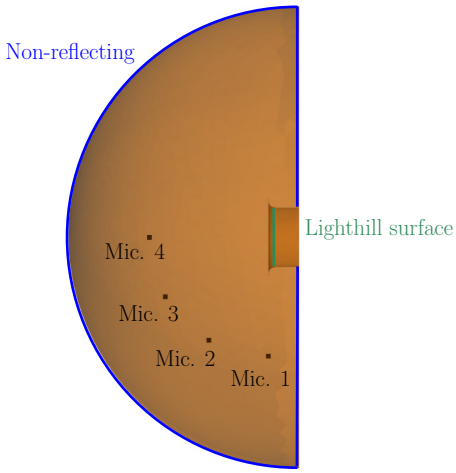

Figure 3.11: Computational domain top view.

To mimic the non-reflecting radiation condition, infinite element boundary condition is applied to the outer boundary of the acoustic domain. To improve the accuracy of

the infinite element condition, the shape of the inlet domain is changed from cuboid to hemisphere; see Fig. 3.11. Infinite element method is well known to be useful in boundary value problems defined in unbounded computational domains, more information about infinite element method and its formulation can be found in [23].

3.2.3 Measuring points

Following the measurement setup, four probes are arranged on a shape of semicircle with a radius of 1m centered around the inlet nozzle and at the same height of the rotational axis. The probes are placed at the suction side of the fan as can be seen in Fig. 3.11.

4

Results & Discussion

The numerical results obtained from the CFD and the CAA simulations are presented in this chapter. The comparison between the numerical results and the experimental data is also discussed.
The experimental results used as a benchmark case for this project are from the study conducted by Zenger et al. [2]. The detailed measurement setup and the general test chamber properties are described in [2]. The axial fan design parameters are calculated using the blade element/ momentum method (BEMM). A short summary of BEMM theory and our implementation of the method are presented in Appendix B.

4.1 Steady state simulation

The main purpose of the steady simulation is to compare different models and mesh structures using MRF approach, before going further to the main unsteady simulation. Pressure rise across the fan and velocity profile along the rotor blade are presented.

4.1.1 Pressure difference

Tab. 4.1 shows the pressure difference across the fan for different turbulence models and mesh structures. The SST $k-\omega$ model with polyhedral mesh and the realizable $k-\varepsilon$ model with trimmed mesh show good estimations of the pressure difference with a deviation of 0.31% and 0.79% from measurement value, respectively. On the other hand, the realizable $k-\varepsilon$ model with polyhedral mesh give a relatively far estimation with a deviation of 7.8%.

	Pressure difference (Pa)
Measurement	126.5
Realizable $k-\varepsilon$/Polyhedral mesh	116.6
Realizable $k-\varepsilon$/Trimmed mesh	125.5
SST $k-\omega$/Polyhedral mesh	126.9

Table 4.1: Pressure difference for different steady simulation models.

4.1.2 Axial velocity

Both the realizable $k-\varepsilon$ and the SST $k-\omega$ models overestimate the axial velocity along the rotor blade on the suction side, except for a lower velocity prediction for the realizable $k-\varepsilon$ model at the blade tip. At the pressure side, the axial velocity values for both models are in the same range as the measured ones except for a noticeable overestimation before reaching the tip region for the SST $k-\omega$ model. This poor prediction of the axial velocity profile is probably because of the the small volume size of the MRF rotational domain as discussed by Gullberg et al. [24].
For different mesh structures with the realizable $k-\varepsilon$ turbulence model, trimmed mesh gives a smoother velocity profile at both fan sides. Further mesh refinements are applied to $k-\varepsilon$ model to check the possibility of obtaining more accurate results. The refinements include

- decreasing minimum cell size to half of the value used in the original mesh,
- increasing mesh density by 20%,
- decreasing mesh growth rate by 20%.

Fig. 4.3 shows the axial velocity profile, $\langle U_x \rangle$, of the different mesh refinements methods. It can be seen that there is no crucial difference between any of the refinements and the original mesh. However, decreasing the minimum cell size does improve the prediction of the axial velocity at the tip and the hub of the blade at the pressure side of the fan. Nevertheless, comparing this improvement to the number of extra cells (around 8 million) added for the mesh refinement, it is concluded that it would be more computationally efficient to proceed with the original mesh structure for further simulations.

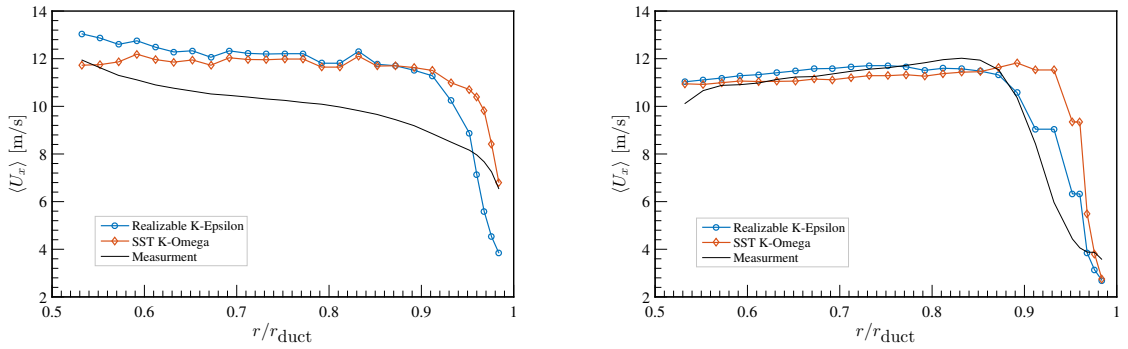

(a) Suction side.

(b) Pressure side.

Figure 4.1: Axial mean velocity profile $\langle U_x \rangle$ for different turbulence models.

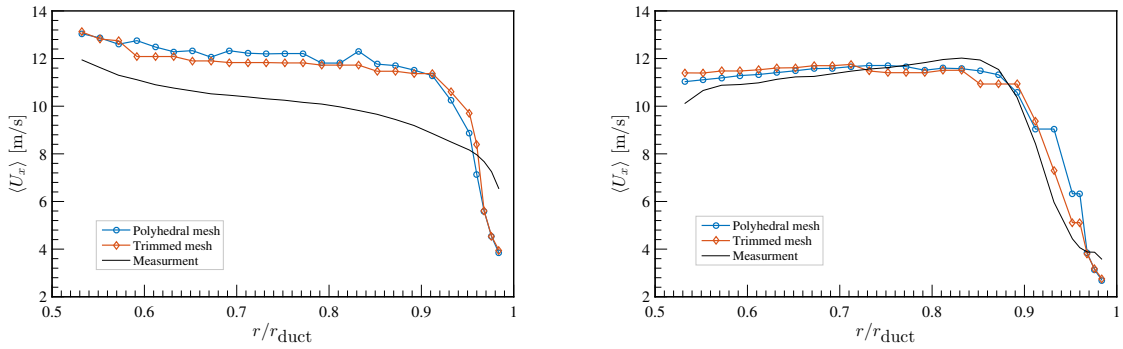

(a) Suction side. (b) Pressure side.

Figure 4.2: Axial velocity profile $\langle U_x \rangle$ for different mesh structures.

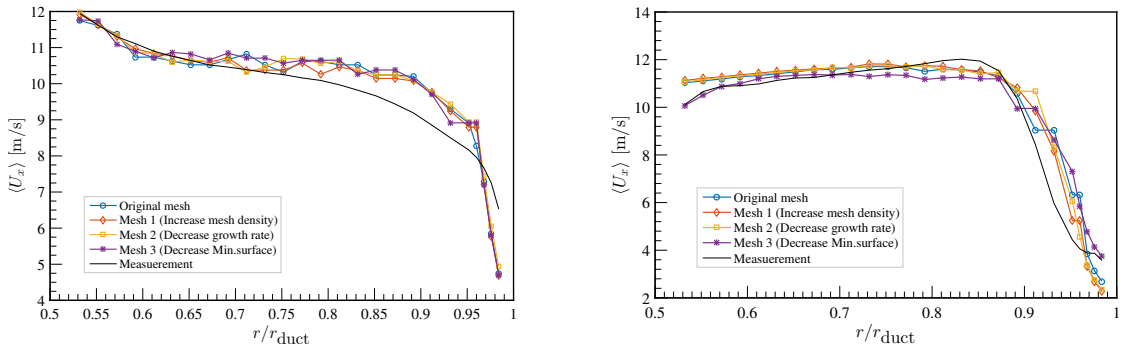

(a) Suction side. (b) Pressure side.

Figure 4.3: Axial velocity profile $\langle U_x \rangle$ for different mesh refinements.

4.2 Unsteady state simulation

The URANS results are extracted after passing 2 seconds of simulation time which corresponds to 50 fan revolutions. The total export time of the results is around 0.7s which is equivalent to 17 revolutions. Data are exported at each time step(Δt = 0.1ms). Time averaged pressure difference, axial velocity profile and wall pressure fluctuations are presented in the next sections.

4.2.1 Pressure difference

The time averaged pressure difference values for the realizable $k-\varepsilon$ model with both polyhedral and trimmed mesh show a close estimation to the measurement value with a deviation of 2.4% and 1.2% respectively, while the SST $k-\omega$ model with polyhedral mesh gives a relatively poorer estimation with a deviation of 4.2% as can be seen in Tab. 4.2.

4.2.2 Axial velocity

The time averaged axial velocity results for both turbulence models at the suction side give a good overall axial velocity profile values against the measured ones with an

	Pressure difference (Pa)
Measurement	126.5
Realizable $k-\varepsilon$/Polyhedral mesh	123.4
Realizable $k-\varepsilon$/Trimmed mesh	128.06
SST $k-\omega$/Polyhedral mesh	131.9

Table 4.2: Pressure difference for different unsteady simulation models.

overestimation after the middle part of the blade and a remarkable underestimation at the tip region as shown in Fig. 4.4(a). For the pressure side, the realizable $k-\varepsilon$ model slightly underestimates the velocity value at the middle region of the blade and gives a close prediction of the flow velocity at blade tip. The SST $k-\omega$ model gives a poor velocity profile quality compared to the realizable $k-\varepsilon$ model with a similar behavior at the middle region of the blade, higher overestimation after the middle part and a steep decrease in the velocity value at the hub region as can be seen in Fig. 4.4(b). Furthermore, the study for different wall treatments in RANS models in Appendix A shows that the realizable $k-\varepsilon$ with all y^+ treatment accuracy is less sensitive than the SST $k-\omega$ with all y^+ treatment at near-wall y^+ values. For different mesh types with realizable $k-\varepsilon$ turbulence model, both polyhedral and trimmed mesh give similar velocity profile predictions at the suction side (see Fig. 4.5(a)); however, trimmed mesh gives completely far prediction of the velocity profile at the pressure side as shown in Fig. 4.5(b). In general, The unsteady simulation gave a better prediction to the velocity profile at the suction side but not for the pressure side compared to the steady simulation.

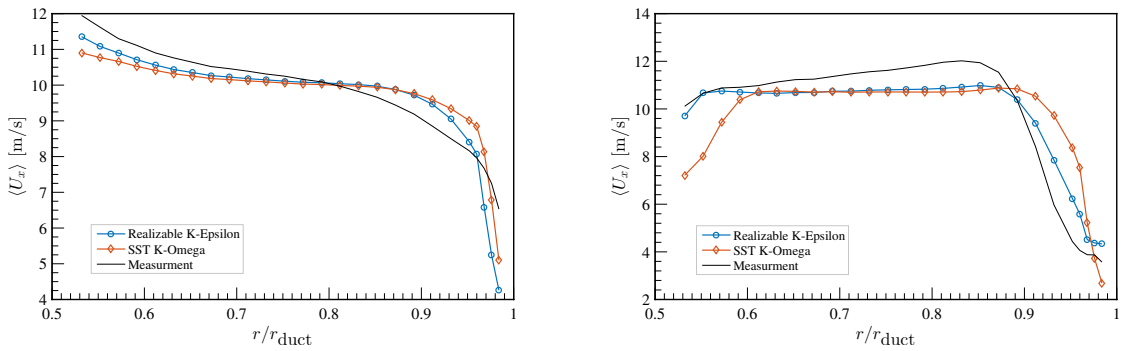

(a) Suction side.

(b) Pressure side.

Figure 4.4: Time averaged axial velocity profile for different turbulence models.

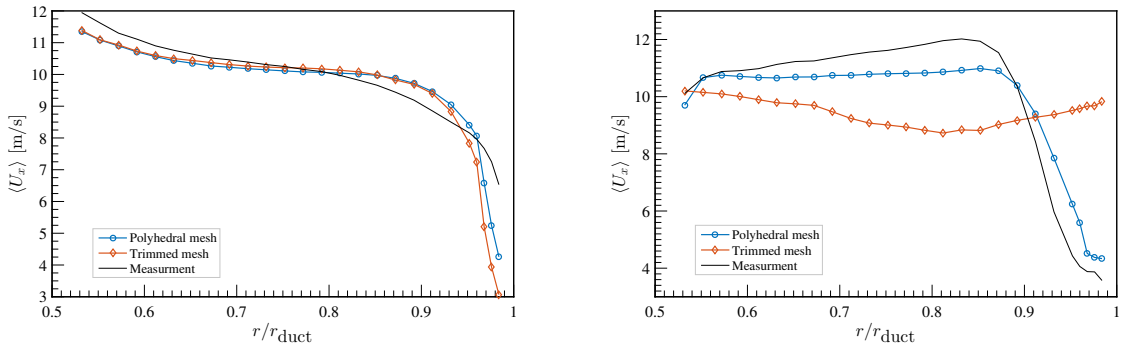

(a) Suction side.

(b) Pressure side.

Figure 4.5: Time averaged axial velocity profile for different mesh structures.

4.2.3 Wall pressure fluctuations

After comparing velocity profiles at suction and pressure sides of the fan for different simulation models, the realizable $k-\varepsilon$ model with polyhedral mesh is concluded to be the most convenient model to use for further simulation investigations. Wall pressure fluctuations are measured in the fan duct as described in Sec. 3.1.6. The power spectral density (PSD) of wall pressure fluctuations are calculated using Matlab's function "pwelch" (The Mathworks, R2015a) with hanning window and 50% overlap ratio. The PSD of the acoustic signal measured by the four different probes are shown in Fig. 4.6 where probe 2 is located before the blades on the suction side. Probe 7 & 8 are located in the same line with the blades and probe 14 is located after the blades at the pressure side. Since URANS model is used, results focus only on the narrow-band components of the fan noise and ignore the broad-band components. The simulation succeeded to resolve the blade passing frequency at 225Hz with a slight overestimation at the probes locations except for probe 14. The sub-harmonic peak at 335Hz is expected to be caused by the interaction of the gap flow with the fan blades as described in [25], the simulation greatly overestimates this sub-harmonic peak at the four probes locations.

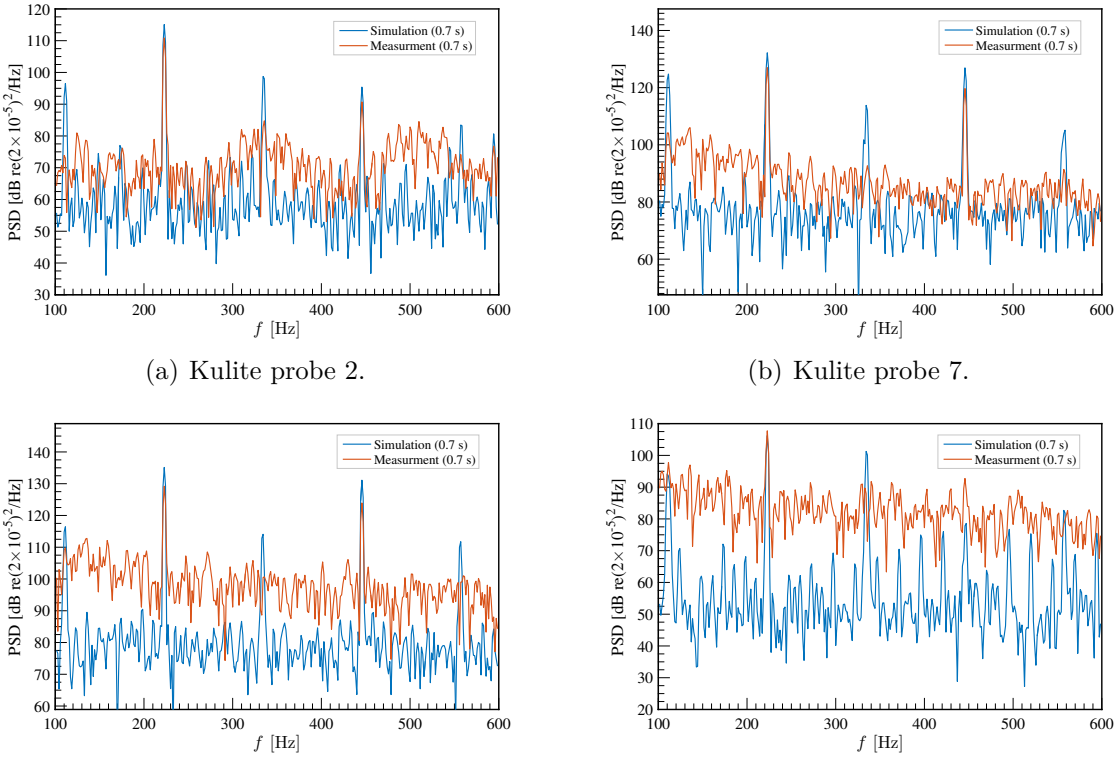

(a) Kulite probe 2.

(b) Kulite probe 7.

(c) Kulite probe 8.

(d) Kulite probe 14.

Figure 4.6: PSD of wall pressure probes at the fan duct.

4.3 CAA simulation

The acoustic signal is measured at the suction side of the fan as described in Sec. 3.2.3. The sound pressure level of the simulation acoustic signal is calculated in the frequency domain by Actran using iCFD tool. Signal processing properties used are similar to the ones described for wall pressure fluctuations. Unfortunately, due to the unavailability of measurement data, measurement results are scanned electronically from Junger numerical study [6]. Fig. 4.7 shows The PSD of the four microphones described in Fig. 3.11. Similar to wall pressure fluctuations, low frequency results are only presented. The simulation successfully reproduce blade passing frequency with an underestimation at the four microphone locations while overestimates the sub-harmonic peak at 335Hz at all microphone locations except for microphone 4, the PSD is highly underestimated. The acoustic signal behaviour at microphone 4 is probably because of the simulation representation to the acoustic source as a dipole source as can be clearly seen in the Lighthill's surface density contour at 335Hz in Fig. 4.8. Acoustic simulation results at the first three microphones show a good prediction of the PSD at the blade passing frequency compared to the detached eddy simulations (DES) used by Junger [6] through OpenFOAM and Fluent for the same benchmark case.

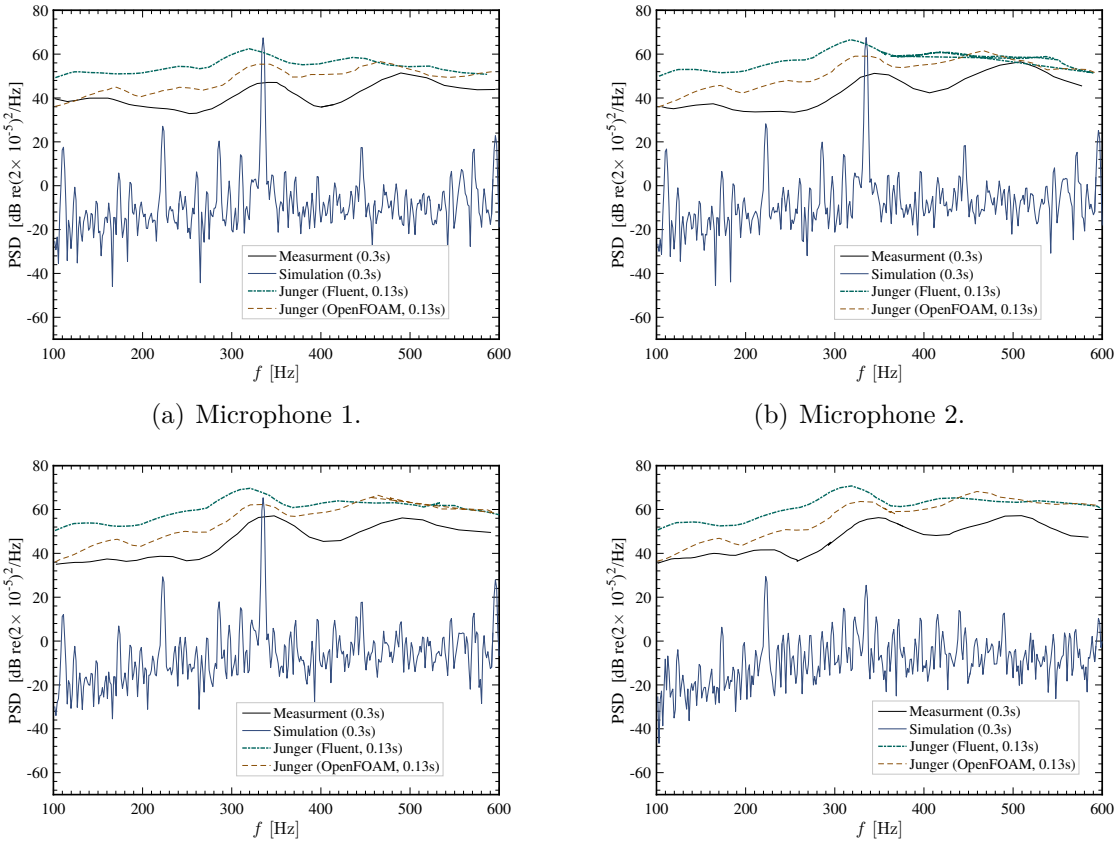

(a) Microphone 1.

(b) Microphone 2.

(c) Microphone 3.

(d) Microphone 4.

Figure 4.7: PSD of the acoustic signal.

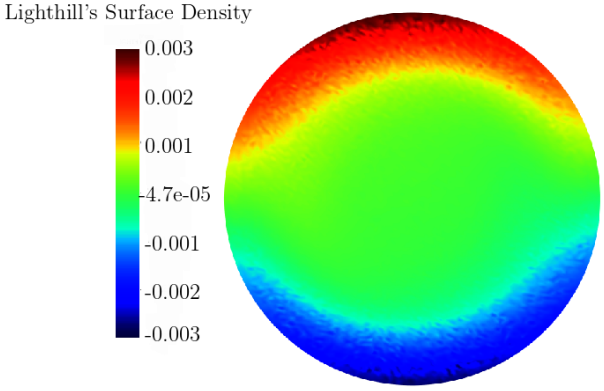

Figure 4.8: Lighthill surface density at 335Hz.

5
Conclusion

The low-pressure axial fan benchmark case published in Zenger et al. [2] has been reproduced numerically and the aerodynamic and the narrow-band acoustic results have been compared with the measurement results.
The steady RANS CFD model has been first applied using MRF approach to calculate the mean flow field and compare different simulation models and mesh structures. The pressure rise of the fan and the axial velocity profile at both sides of the fan have shown good agreement with the measurement data provided by Zenger et al. [2]. No major differences have been noticed for different mesh refinements applied to the steady state simulation model. The calculated mean flow has later been used by the URANS CFD model as initial conditions.
The URANS models have been applied using sliding mesh approach for fan modeling. The realizable k-ε URANS model with polyhedral mesh has provided good prediction of the mean flow quantities. In addition, the unsteady wall pressure fluctuations computed, have succeeded to resolve the fan blade passing frequency and the subharmonic frequency resulted from the interaction of the gap flow with the fan blades. The calculated unsteady flow field has later been used as a surface noise source to analyze the aerodynamically generated noise through Lighthill's analogy. The narrow-band acoustic components of the fan noise have been successfully captured, although the predicted power spectrum density has been severely underestimated at several measurement points. Compared to other numerical simulation models applied for the same benchmark case, the simulation model presented gave a good prediction to the acoustic signal.
Overall, the presented approach has been shown to be able to provide promising results in resolving the narrow-band noise spectrum. The next step is to extend the approach to predict the broad-band components by employing more advanced CFD models, such as the large eddy simulation.

Bibliography

[1] Chenyang Weng. Volvo internal report 19w24: Implementation of the blade element/momentum method. Technical report, Volvo Car Group, Powertrain NVH CAE and P&D, Torslanda SE-40531 Göteborg, Sweden, June 2019.

[2] Florian Zenger, Clemens Junger, Manfred Kaltenbacher, and Stefan Becker. A benchmark case for aerodynamics and aeroacoustics of a low pressure axial fan. In *9th International Styrian Noise, Vibration & Harshness Congress: The European Automotive Noise Conference*. SAE International, jun 2016. doi: https://doi.org/10.4271/2016-01-1805.

[3] S. Khelladi, S. Kouidri, F. Bakir, and R. Rey. Predicting tonal noise from a high rotational speed centrifugal fan. *Journal of Sound and Vibration*, 313(1):113 – 133, 2008. ISSN 0022-460X. doi: https://doi.org/10.1016/j.jsv.2007.11.044.

[4] Anders Rynell, Mattias Chevalier, Mats Åbom, and Gunilla Efraimsson. A numerical study of noise characteristics originating from a shrouded subsonic automotive fan. *Applied Acoustics*, 140:110 – 121, 2018. ISSN 0003-682X. doi: https://doi.org/10.1016/j.apacoust.2018.05.006.

[5] Manfred Kaltenbacher, Andreas Hüppe, Aaron Reppenhagen, Florian Krömer, and S Becker. Computational aeroacoustics for rotating systems with application to an axial fan. *AIAA Journal*, 55, 09 2017. doi: 10.2514/1.J055931.

[6] Clemens Junger, Florian Krömer, Aaron Reppenhagen, Manfred Kaltenbacher, and S Becker. Numerical simulation of a benchmark case for aerodynamics and aeroacoustics of a low pressure axial fan. 08 2016.

[7] Bengt Andersson, Ronnie Andersson, Love Håkansson, Mikael Mortensen, Rahman Sudiyo, and Berend van Wachem. Computational fluid dynamics for engineers. Cambridge University Press, 2011. doi: 10.1017/CBO9781139093590.

[8] J.O. Hinze. Turbulence:. McGraw-Hill classic textbook reissue series. McGraw-Hill, 1975. URL `https://books.google.se/books?id=DfRQAAAAMAAJ`.

[9] B. E. Launder and D. B. Spalding. *Lectures in mathematical models of turbulence*. Academic Press London, New York, 1972. ISBN 0124380506.

[10] Siemens.PLM.software. Star-ccm+ user's guide.version 11.06.010. 2016.

[11] D.C. Wilcox. *Turbulence Modeling for CFD*. Number v. 1 in Turbulence Modeling for CFD. DCW Industries, 2006. ISBN 9781928729082.

[12] F. R. Menter. Two-equation eddy-viscosity turbulence models for engineering applications. *AIAA Journal*, 32(8):1598–1605, 1994. doi: 10.2514/3.12149.

[13] ANSYS. Fluent 12.0 theory guide. 2009.

[14] A. Hirschberg and S. W. Rienstra. An introduction to aeroacoustics. Technical report, Eindhoven University of Technology, 2004.

[15] C.L. Morfey. Amplification of aerodynamic noise by convected flow inhomogeneities. *Journal of Sound and Vibration*, 31(4):391–397, 12 1973. doi: 10.1016/S0022-460X(73)80255-X.

[16] MSC software company Free Field Technologies. Actran 18.0 installations, operations, theory and utilities user's guide. 2017.

[17] Assad A Oberai, Farzam Roknaldin, and Thomas J.R Hughes. Computational procedures for determining structural-acoustic response due to hydrodynamic sources. *Computer Methods in Applied Mechanics and Engineering*, 190:345 – 361, 10 2000. doi: 10.1016/S0045-7825(00)00206-1.

[18] D. G. Crighton. Aeroacoustics. by marvin e. goldstein. mcgraw-hill, 1976. 293 pp. £16.45. *Journal of Fluid Mechanics*, 83(2):396–400, 1977. doi: 10.1017/S0022112077211256.

[19] N. Curle. The influence of solid boundaries upon aerodynamic sound. *Proceedings of the Royal Society of London A: Mathematical, Physical and Engineering Sciences*, 231(1187):505–514, 1955. ISSN 0080-4630. doi: 10.1098/rspa.1955.0191.

[20] S. Howe. *Theory of Vortex Sound*. Cambridge Texts in Applied Mathematics. Cambridge University Press, 2003. ISBN 9780521012232.

[21] Kenneth S. Brentner and F. Farassat. Analytical comparison of the acoustic analogy and kirchhoff formulation for moving surfaces. *AIAA Journal*, 36(8):1379–1386, 1998. doi: 10.2514/2.558.

[22] Dendy Satrio, I Ketut Utama, and Mukhtasor M. The influence of time step setting on the cfd simulation result of vertical axis tidal current turbine. *JOURNAL OF MECHANICAL ENGINEERING AND SCIENCES*, 12:3399–3409, 03 2018. doi: 10.15282/jmes.12.1.2018.9.0303.

[23] KLAUS GERDES. A review of infinite element methods for exterior helmholtz problems. *Journal of Computational Acoustics - J COMPUT ACOUST*, 8:43–62, 03 2000. doi: 10.1016/S0218-396X(00)00004-2.

[24] Peter Gullberg, Lennart Löfdahl, Peter Nilsson, and Steven Adelman. Continued study of the error and consistency of fan cfd mrf models. 04 2010. doi: 10.4271/2010-01-0553.

[25] Stéphan Magne, Stéphane Moreau, and Alain Berry. Subharmonic tonal noise from backflow vortices radiated by a low-speed ring fan in uniform inlet flow. *The Journal of the Acoustical Society of America*, 137 1:228–37, 2015.

[26] Chenyang Weng, Susann Boij, and Ardeshir Hanifi. Numerical and theoretical investigation of pulsatile turbulent channel flows. *Journal of Fluid Mechanics*, 792:98–133, 4 2016. ISSN 1469-7645. doi: https://doi.org/10.1017/jfm.2016.73.

[27] Stefano Castegnaro. Aerodynamic design of low-speed axial-flow fans: A historical overview. *Designs*, 2(3), 2018. ISSN 2411-9660. doi: 10.3390/designs2030020.

[28] Jens Nørkær Sørensen. *Blade–Element/Momentum Theory*, pages 99–121. Springer International Publishing, Cham, 2016. ISBN 978-3-319-22114-4. doi: 10.1007/978-3-319-22114-4_7.

[29] Manelisi Kagame Rwigema. Propeller blade element momentum theory with vortex wake deflection. In *27th Congress of International Council of the Aeronautical Sciences, Nice, France*. Paper ICAS 2010-2.3.3, 2010.

[30] Eric Jones, Travis Oliphant, Pearu Peterson, et al. SciPy: Open source scientific tools for Python, 2001–. URL `http://www.scipy.org/`. [Online; accessed Friday, 14 June 2019].

[31] Mark Drela. Xfoil: An analysis and design system for low reynolds number airfoils. In Thomas J. Mueller, editor, *Low Reynolds Number Aerodynamics*, pages 1–12, Berlin, Heidelberg, 1989. Springer Berlin Heidelberg. ISBN 978-3-642-84010-4.

[32] Pedro B. Camara Leal. Aeropy: Alpha version, February . [Online; accessed Friday, 14 June 2019].

[33] J.D. Anderson. *Fundamentals of Aerodynamics*. McGraw-Hill Education, 5th edition, 2010. ISBN 9780073398105.

[34] Thomas H. Carolus and Ralf Starzmann. An aerodynamic design methodology for low pressure axial fans with integrated airfoil polar prediction. In *ASME 2011 Turbo Expo: Turbine Technical Conference and Exposition, Vancouver, British Columbia, Canada*, volume 4, pages 335–342. Paper No. GT2011-45243, 2011. doi: 10.1115/GT2011-45243.

A

Appendix: Comparison among different wall treatments in RANS models

The purpose of this simple test[1] is to demonstrate that, the accuracy of the "Two-Layer all y^+ wall treatment" $k-\epsilon$ model provided in STAR-CCM+ seems to be less sensitive to the y^+ value of the cell adjacent to the wall, compared to the other RANS models available in the software.

The flow case being investigated is 2D fully developed channel flow with $Re_\tau = u_* H/\nu$=350, where u_* is the friction velocity, and H is the channel half height. Two mesh setups are compared. One with low y^+ values (< 1) near the wall (see Fig. A.1(a)), the other with medium y^+ values (≈ 10) near the wall (see Fig. A.1(b)). In both setups, prism layer is used in the boundary layer, while poly-mesh is used away from the wall. The no-slip boundary condition is applied at $y = 0$ and the symmetry condition is used at $y = H$. Inlet and outlet boundaries are coupled through the "Fully-Developed Interface".

The mean velocity profiles computed from four RANS models with different wall treatments provided in STAR-CCM+ are compared. They are

1. Realizable $k-\epsilon$, all y^+ treatment.
2. Realizable $k-\epsilon$, high y^+ treatment.
3. SST $k-\omega$, all y^+ treatment.
4. SST $k-\omega$, low y^+ treatment.

The DNS data from [26, Figure 3] are used as the benchmark data. Based on the comparison shown in Fig. A.2 we may draw the following conclusions.

- The SST $k-\omega$ model with either all or low y^+ treatment is accurate only when the low y^+ mesh is employed; its accuracy is deteriorated when the first mesh cell has y^+ value much larger then unity (the SST $k-\omega$ model with low y^+ treatment does not even converge in the case of Fig. A.2(b)).
- The realizable $k-\epsilon$ with high y^+ treatment works properly only for the medium y^+ mesh, but not for the case where the near-wall y^+ value is less than unity.
- The accuracy of the realizable $k-\epsilon$ with all y^+ wall treatment seems to be less sensitive to the near-wall y^+ values.

Since it is generally difficult to know *a priori* the near-wall y^+values for the entire computational domain, it is probably less risky to choose the realizable $k-\epsilon$ model with all y^+ treatment as the first attempt of the simulation.

[1] Being inspired by https://www.youtube.com/watch?v=mVE9OAB5Sao.

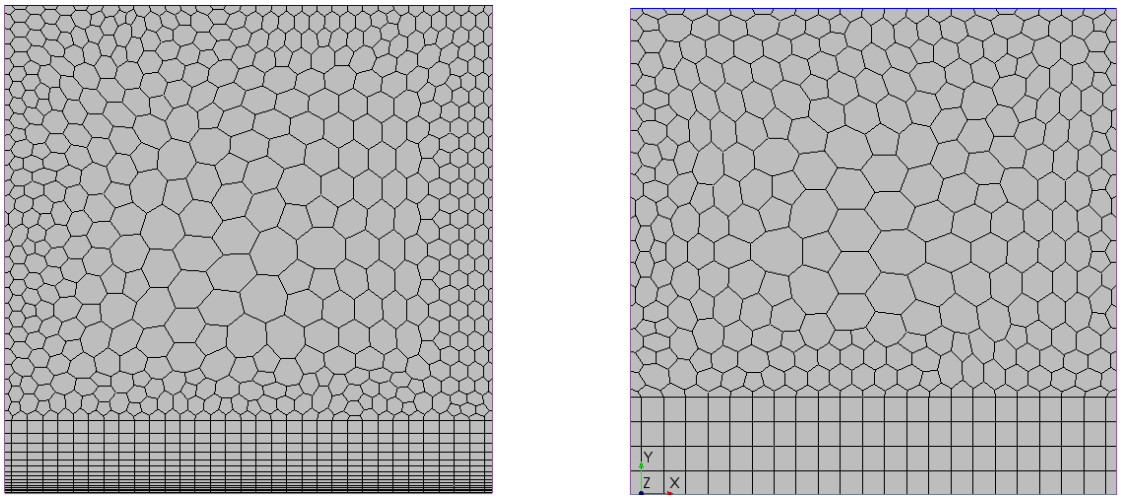

(a) Low y^+ mesh (b) Medium y^+ mesh

Figure A.1: Two mesh setups used in the test case.

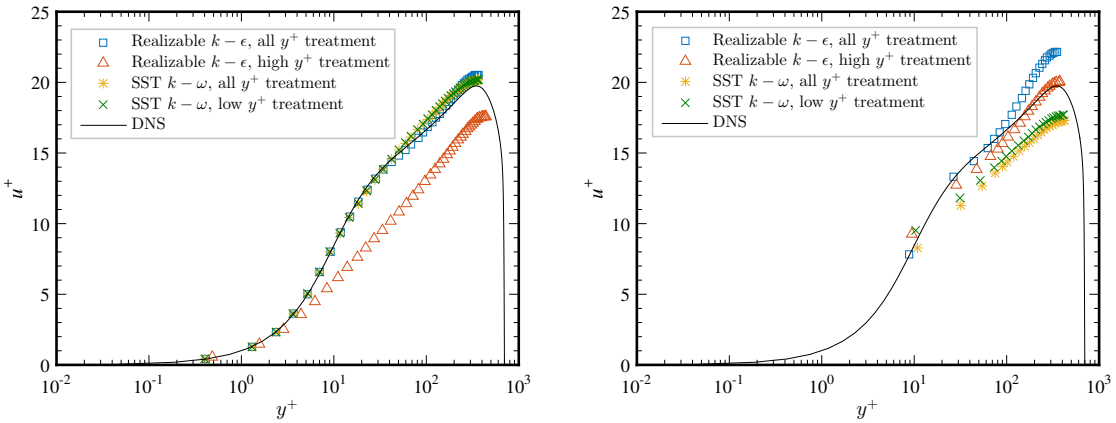

(a) Low y^+ mesh (b) Medium y^+ mesh

Figure A.2: Dimensionless velocity $u^+ = u/u_*$ over y^+. Note that the SST $k-\omega$ model with low y^+ treatment is not converged in the case of Fig. A.2(b).

B

Appendix: Blade element/momentum method (BEMM)

The BEMM can be used in the conceptual design of axial fans [27]. Compared to CFD, the BEMM provides a quick (though less accurate) prediction of the performance of a fan. The method is also very easy to understand and implement. To assist the investigation of cooling-fans on future Volvo electric vehicles, the BEMM is implemented using Python 3 [1]. This chapter summarizes the theory of BEMM and the details of the implementation. The code is applied to the N1UG fan and the results are compared with those given in [2]

B.1 Theory

The BEMM is a combination of the blade element method and the momentum theory [27, 28]. Detailed formulation of the BEMM can be easily found from the internet so it is not repeated here. What is shown in this chapter is merely concise summary of the BEMM.

The fundamental idea behind the BEMM is to divide the fan blades into a number of "blade elements" and perform dynamic analysis locally for each element. The performance of the fan is then evaluated by integrating the local dynamic quantities over all the blade elements.

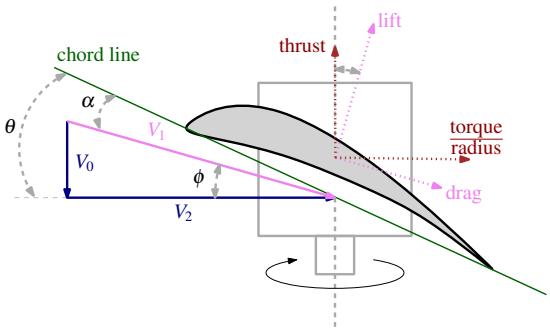

Figure B.1: Sketch of the velocity triangle and force vector on a blade element. Image source: [1], reproduced with permission.

In Fig. B.1 the airfoil profile of an individual blade element is illustrated. Our goal here is to calculate the local thrust and torque from the velocity triangles. For blade elements on an annular ring with radius r and width $\mathrm{d}r$, it can be easily shown that the thrust $\mathrm{d}\mathfrak{T}$ and torque $\mathrm{d}\mathfrak{Q}$ are respectively given by

$$\mathrm{d}\mathfrak{T} = \frac{1}{2}\rho_0 V_1^2 \mathfrak{c} N_\mathrm{B} \left(C_\mathrm{L}\cos\phi - C_\mathrm{D}\sin\phi\right)\mathrm{d}r, \tag{B.1a}$$

and

$$\mathrm{d}\mathfrak{Q} = \frac{1}{2}\rho_0 V_1^2 \mathfrak{c} N_\mathrm{B} \left(C_\mathrm{D}\cos\phi + C_\mathrm{L}\sin\phi\right) r\mathrm{d}r. \tag{B.1b}$$

where $\mathfrak{c}$ is the chord length, N_B is the number of blade, and C_L and C_D are the lift and drag coefficient, respectively. The local inflow V_1 should be determined from the axial flow speed V_0 and the angular flow speed V_2 as

$$V_1 = \sqrt{V_0^2 + V_2^2}. \tag{B.2}$$

If we assume that the velocity at the far-upstream (ambient condition) of the fan is V_∞, then, by taking into account the axial and swirl velocity induced by the fan, we may write the local V_0 and V_2 as

$$V_0 = V_\infty\left(1 + a\right), \tag{B.3}$$

and

$$V_2 = \Omega r\left(1 - b\right), \tag{B.4}$$

where a is the axial inflow factor, and b is the angular inflow factor, and $\Omega = 2\pi \cdot \mathrm{RPM}/60$ is the angular speed of the rotor. To further determine the factors, we need the following relations derived from the momentum theory [29]

$$\mathrm{d}\mathfrak{T} = 4\pi r \rho_0 V_\infty^2 a\left(1 + a\right)\mathrm{d}r, \tag{B.5a}$$

and

$$\mathrm{d}\mathfrak{Q} = 4\pi r^3 \rho_0 V_\infty \Omega b\left(1 + a\right)\mathrm{d}r. \tag{B.5b}$$

By solving Eq. (B.1) and Eq. (B.5) with the two unknowns a and b, we may obtain the total thrust on the fan as $\mathfrak{T} = \int_{r_\mathrm{hub}}^{r_\mathrm{tip}} \mathrm{d}\mathfrak{T}$, which further gives the static pressure rise of the fan (averaged over the area, A, of the fan blades) as $\Delta p = \mathfrak{T}/A$. Due to the assumption of inviscid fluid in the underlying momentum theory, the increase in the total pressure is experienced as an increase in the static pressure Δp at the fan. Since C_L and C_D are generally[1] function of the angle of attack α, given by

$$\alpha = \theta - \phi = \theta - \arctan\frac{V_0}{V_2} = \theta - \arctan\frac{V_\infty\left(1 + a\right)}{\Omega r\left(1 - b\right)}, \tag{B.6}$$

which is also a function of a and b, we may have to solve Eq. (B.1) and Eq. (B.5) iteratively. The implementation of the iteration solver is given in the next section.

B.2 Implementation

The BEMM formulations given by Eq. (B.1) and Eq. (B.5) are solved iteratively with an in-house program written in Python. Several root-finding algorithms are provided as the solver, among which the `fsolve` function in the SciPy library [30] is the most recommended. The lift and drag coefficients C_L and C_D are computed

[1] They are also function of the local Reynolds number in the current implementation because the flow boundary layer at the airfoil is taken into account.

with XFOIL [31], an analysis and design system for low Reynolds number airfoils. The Python interface for XFOIL is built up via the open-source library AeroPy [32]. To accelerate the convergence of the `fsolve` function, the initial guesses for the unknowns a and b are obtained via a fast bisection-like root-finding method where the lift and drag coefficients are computed using the following symmetric-airfoil approximations for small angle of attack [33]:

$$C_{\mathrm{L}} = 2\pi\alpha \text{ and } C_{\mathrm{D}} = 0.01C_{\mathrm{L}}^2 - 0.003C_{\mathrm{L}} + 0.008. \tag{B.7}$$

In spite of the above calculation of the initial guesses, convergence is not always guaranteed while using XFOIL for a given fan geometry. One may need to manually tune the parameters in `fsolve` to achieve the convergence with certain tolerance.

B.3 Application to N1UG fan

The N1UG fan investigated in [2] was designed with an improved blade element theory proposed by Carolus and Starzmann [34]. Their results are compared with the current implementation.
In the current investigation each fan blade is divided into 20 blade elements. The NACA 4501 airfoil is used in XFOIL to compute the local lift and drag coefficients. The computed results are summarized in Tab. B.1. As can be seen, although the geometry-related quantities are somehow different in the two cases, the values of the pressure rise, which is the quantity that interests us the most in fan design, are almost the same.

	Zenger et al. [2]	Current implementation
RPM	1486 min^{-1}	
Volumetric flow	1.4 $\mathrm{m}^3\mathrm{s}^{-1}$	
Chord length hub	103 mm	95.17558 mm
Chord length tip	58 mm	54.61657 mm
Reynolds number hub	$1.25 \cdot 10^5$	$1.38939 \cdot 10^5$
Reynolds number tip	$1.5 \cdot 10^5$	$1.63902 \cdot 10^5$
Pressure rise	150 Pa	147.10902 Pa

Table B.1: Comparison between the N1UG design parameters given in [2] and those reversely computed with the current implementation of the BEMM [1]. The chord lengths are different in the two cases mainly due to the choices of the blade element sizes.